1   # Atmospheric ammonia variability and link with PM formation: a

2   # case study over the Paris area

3   Viatte Camille[1], Wang Tianze[1], Van Damme Martin[2], Dammers Enrico [3], Meleux Frederik[4],

4   Clarisse Lieven[2], Shephard Mark W.[3], Whitburn Simon[2], Coheur Pierre François[2], Cady-Pereira

5   Karen E.[5], and Clerbaux Cathy[1,2]

6   [1] LATMOS/IPSL, Sorbonne Université, UVSQ, CNRS, Paris, France
7   [2] Université libre de Bruxelles (ULB), Service de Chimie Quantique et Photophysique, Atmospheric
8   Spectroscopy, Brussels, Belgium
9   [3] Environment and Climate Change Canada, Toronto, Ontario, Canada
10 [4] Institut national de l'environnement industriel et des risques, INERIS, Verneuil en Halatte, France
11 [5] Atmospheric and Environmental Research (AER), Inc., Lexington, USA

Atmospheric
Chemistry
and Physics
Discussions

Open Access

Abstract

The Paris megacity experiences frequent particulate matter ($PM_{2.5}$, PM with a diameter less than 2.5 μm) pollution episodes in springtime (March-April). At this time of the year, large parts of the particles consist of ammonium sulfate and nitrate which are formed from ammonia (NH_3) released during fertilizer spreading practices and transported from the surrounding areas to Paris. There is still limited knowledge on the emission sources around Paris, their magnitude and seasonality.

Using space-borne NH_3 observation records of 10-years (2008-2017) and 5-years (2013-2017) provided by the Infrared Atmospheric Sounding Interferometer (IASI) and the Cross-Track Infrared Sounder (CrIS) instrument, regional pattern of NH_3 variabilities (seasonal and inter-annual) are derived. Observations reveal identical high seasonal variabilities with three major NH_3 hot spots found from March to August. The high inter-annual variability is discussed with respect to atmospheric total precipitation and temperature.

A detailed analysis of the seasonal cycle is performed using both IASI and the CrIS instrument data, together with outputs from the CHIMERE atmospheric model. For months of high NH_3 concentrations (March to August) the CHIMERE model shows good correspondence with correlation slopes of 0.98 and 0.71 when comparing with IASI and CrIS, respectively. It is found that the model is only able to reproduce half of the observed atmospheric temporal NH_3 variability in the domain. In term of spatial variability, the CHIMERE monthly NH_3 concentrations in springtime show a slight underrepresentation over Belgium and the United-Kingdom and overrepresentation in agricultural areas in the French Brittany/Pays de la Loire and Plateau du Jura region, as well as in the north part of Switzerland.

Using HYSPLIT cluster analysis of back-trajectories, we show that NH_3 total columns measured in spring over Paris are enhanced when air masses are originated from the Northeast (e. g., Netherlands and Belgium), highlighting the long-range transport importance on the NH_3 budget over Paris.

Finally, we quantify the key meteorological parameters driving the specific conditions important for the $PM_{2.5}$ formation from NH_3 in the Ile-de-France region in springtime. Data-driven results based on surface $PM_{2.5}$ measurements from the Airparif network and IASI NH_3 observations show that a combination of the factors, e. g. a low boundary layer of ~500m, a relatively low temperature of 5°C and a high relative humidity of 70%, contributes to favor $PM_{2.5}$ and NH_3 correlation.

Atmospheric
Chemistry
and Physics
Discussions

1. Introduction

Ammonia (NH$_3$) is an atmospheric pollutant and one of the main sources of reactive nitrogen in the atmosphere which is involved in numerous biochemical exchanges impacting all ecosystems [Sutton et al., 2013]. The global budget of reactive N has dramatically increased since the preindustrial era [Holland et al., 2005; Battye et al., 2017] causing major environmental damages such as ecosystems and species extinction, as well as soil and water eutrophication and acidification [Rockström et al., 2009]. NH$_3$ is a precursor of ammonium salts which can form up to 50% to particulate matter (PM) total mass [Behera et al., 2013]. Large cities such as Paris (which is the most populated area in the European Union with 10.5 million people when its larger metropolitan regions are included) typically experiences strong PM pollution episodes in springtime. These particles are known to be harmful for human health [Pope III et al., 2009] inducing 2000 deaths per year in the Paris megacity [Corso et al., 2016] and to impact the radiative budget of the Earth [Myhre et al., 2013].

Because of their impact on the environment, public health, and climate change, NH$_3$ emissions are regulated in several countries in the world. However, NH$_3$ emissions of European countries have increased by 2% over the period 2014-2016 [National Emission Ceilings Directive reporting status, 2018], where the Gothenburg Protocol set a reduction of 6% by 2020. In France, where 94% of NH$_3$ emissions come from the agriculture sector [CITEPA, 2018] as a result of extensive fertilizer use to increase crop yields [Erisman et al., 2008], policies have been implemented with the aim to reduce NH$_3$ emissions by 13% in 2030 related to 2005 [CEIP, 2016]. However NH$_3$ emissions are projected to increase in the future globally with increased population and food demand [van Vuuren et al., 2011] and NH$_3$ volatilization will be enhanced with climate change [Sutton et al., 2013].

Once in the atmosphere, NH$_3$ is rapidly removed by wet and dry deposition, and by reactions with atmospheric sulfuric and nitric acid, leading to a relatively short lifetime between a few hours and few days [Galloway et al., 2003]. Release of NH$_3$ in the atmosphere depends on i) agriculture practices: spreading season, fertilizer form (urea, ammonium nitrate), fertilizer application methods, crops, soil conditions such as pH [Hamaoui-Laguel et al., 2014]; and on ii) meteorological conditions (i.e. wind, temperature, and precipitation). Inter-annual variability of PM formation over urban area is poorly understood, since it also depends on many factors such as atmospheric humidity and temperature, which govern the phase equilibrium of secondary aerosols [Fuzzi et al., 2015]. The variety of factors influencing NH$_3$ volatilization and PM formation illustrates the complexity of predicting their concentrations in the atmosphere [Behera et al., 2013].

Atmospheric chemical transport models have difficulty representing both NH$_3$ and PM$_{2.5}$ distributions due to the challenge of reproducing NH$_3$ temporal variability [Pinder et al., 2006;

Atmospheric
Chemistry
and Physics
Discussions

Open Access

EGU

80   Fortems-Cheiney et al., 2016], long-range transport of pollutants [Moran et al., 2014], and
81   secondary aerosol formation in the atmosphere [Petetin et al., 2016]. The GEOS-Chem chemical
82   transport model [Bey et al., 2001] was found to underestimate the observed NH_3 concentrations
83   in most regions of the globe [Zhu et al., 2013; Li et al., 2017]. Heald et al. (2012) compared the
84   IASI observations with the GEOS-Chem model and showed that NH_3 is likely underestimated in
85   California, leading to a local underestimate of ammonium nitrate aerosol. Similarly, the French
86   CHIMERE model [Menut et al., 2013] underestimates the NH_3 budget over Paris [Petetin et al.,
87   2016; Fortems-Cheiney et al., 2016] because of the mis-representation of agricultural emissions
88   in terms of intensity and both spatial and temporal distribution. Often ground and aircraft-
89   based observations are used to provide detailed representation of the atmospheric state that
90   can be used to evaluate and improve the model simulations; however, these can be spatially
91   sparse and/or over short sampling periods, especially globally. Additionally, more recently
92   available (within the last 10-years) sun-synchronous satellite-based infrared sensors have been
93   providing NH_3 observations globally with a spatial resolution of ~15 km approximately twice a
94   day. These satellite observations have limited independent vertical information, but do capture
95   the spatiotemporal variabilities needed to help address these issues and improve model
96   simulations, especially in remote locations [Skjøth et al., 2011; Kranenburg et al., 2016].

97   Aside from the Tropospheric Emission Spectrometer (TES, [Beer et al., 2008]), now
98   decommissioned but which was first to demonstrate the capability of thermal infrared
99   instruments to monitoring lower tropospheric NH_3 , 3 missions are able to measure it now : the
100 Atmospheric InfraRed Sounder (AIRS, [Warner et al., 2016]), the Cross-track Infrared Sounder
101 (CrIS, [Shephard and Cady-Pereira, 2015]), and the Infrared Atmospheric Sounding
102 Interferometer (IASI, [Clarisse et al., 2009]). Recent studies have shown the increased capacity
103 of space-borne instruments to derived spatial and seasonal distributions of NH_3 concentrations
104 globally [Clarisse et al., 2009; Shephard et al., 2011; Van Damme et al., 2014a & 2015a],
105 regionally [Beer et al., 2008; Clarisse et al., 2010; Van Damme et al., 2014b] and locally [Van
106 Damme et al., 2018], as well as trends of NH_3 [Warner et al., 2017].

107 Representative measurements of NH_3 concentrations and spatiotemporal variabilities are
108 needed to address the link between NH_3 and $PM_{2.5}$ formation and improve model simulations.
109 This has been attempted previously in some cities around the world, such as in Shanghai [Ye et
110 al., 2011], Houston [Gong et al., 2013], Santiago City [Toro et al., 2014], and Beijing [Zhao et al.,
111 2016] for instance. However, although the Paris megacity is repeatedly shrouded by particulate
112 pollution episodes, many of studies are limited and performed over relatively short time frame
113 during field campaigns [Petetin et al., 2016; Zhang et al., 2013], or based on numerical
114 simulations [Skyllakou et al., 2014]. Our study is a data-driven regional approach and considers a
115 longer time period to study the seasonal/inter-annual variabilities of NH_3 and its impact of $PM_{2.5}$
116 formation over the Paris megacity. Specifically in this paper we study concentrations and

Atmospheric
Chemistry
and Physics
Discussions

117   spatiotemporal variability of atmospheric NH$_3$ from the agricultural sector to gain insights on its
118   effects on megacity air quality using: 1) long-term satellite observations derived from IASI (10
119   years from 2008 to 2017) and CrIS (5 years from 2013 to 2017) at regional scale (400km radius-
120   circle from Paris city center); 2) spatiotemporal patterns of the CHIMERE model evaluated
121   against the IASI and CrIS datasets for 2014 and 2015; and 3) the main meteorological
122   parameters favoring the secondary PM$_{2.5}$ formation from NH$_3$ in the Paris megacity are
123   analyzed.

2. Methodology

2.1. Region of analysis

126   The domain of analysis covers a circular area of 400 km radius around the Paris city center
127   (Figure 1, larger circle) enabling the study of temporal and spatial variabilities of NH$_3$ emission
128   sources likely to affect air quality in the Paris megacity. It has been selected for two reasons.
129   First, it includes main regions known for their high NH$_3$ emissions, which can be transported and
130   affect air quality over the Parisian region (Ile-de-France –IdF-, smaller circle in Figure 1).
131   Emission regions in the Netherlands, North of Germany, Northwest of Belgium, and the Brittany
132   region in France, are highlighted in darker colors in Figure 1 (emissions values are from the
133   European Monitoring and Evaluation Programme -EMEP- 2015). Second, this area corresponds
134   to the transport of 24 hours back-trajectories from Paris generated from the HYSPLIT model for
135   one year, ensuring that NH$_3$ can indeed be efficiently transported from the emitting sources
136   within the selected domain to the IdF region.

2.2. Satellite observations of ammonia

138   For this study we used the available date from IASI and CrIS which are both Fourier transform
139   spectrometers to evaluate the current capacity to observe NH$_3$ concentrations from space, and
140   study its variability around IdF. Technical information are summarized in Table 1.

2.2.1. Infrared Atmospheric Sounding Interferometer (IASI)

142   IASI is a nadir-viewing spectrometer launched on board the Metop-A and Metop-B satellites and
143   operated by EUMETSAT (European Organisation for the Exploitation of Meteorological
144   Satellites), since October 2006 and September 2012, respectively. These satellites are on similar
145   polar orbits with Equator crossing times at 09:30 (21:30) local mean solar time for the
146   descending (ascending) orbit. IASI measures the thermal infrared radiation of the system Earth-
147   atmosphere in the spectral range from 645 to 2760 cm^{-1} with a spectral resolution 0.5 cm^{-1}
148   apodized. The satellite swath is an area of 2200 km width composed by off-nadir measurements
149   up to 48.3° on both sides of the track. At nadir, the IASI field of view is composed of 4 x 4 pixels
150   of 12 km diameter each [Clerbaux et al., 2009].

Atmospheric
Chemistry
and Physics
Discussions

151 The NH$_3$ total columns used here are derived from IASI using an Artificial Neural Network
152 reanalyzed with ERA-interim data (ANNI-NH3-v2.1R [Van Damme et al., 2017]). This dataset is
153 consistent in time and suitable for investigating inter-annual variability, which is one purpose of
154 this study. Note that we have considered here only morning measurements (9:30) since the
155 evening ones (21:30) are associated with larger relative errors [Van Damme et al., 2017]. IASI
156 retrievals provide a robust error estimate for each IASI-NH3 observations, allowing to take into
157 account the variable sensitivity when comparing IASI dataset with independent measurements.
158 Finally, no filter on relative errors of the IASI datasets has been applied following
159 recommendations from Van Damme et al. (2017) and outliers for which concentrations exceed
160 10 standard deviations above the mean in the domain of study have been removed.

161 Over the studied area, Metop-A and Metop-B have an overpass time difference ranging from
162 only a few seconds to 67 minutes depending on the viewing geometry of the satellite scans; the
163 average difference is 26 minutes for the 1325 days of common measurements. Monthly maps
164 for the 10 years of observations between 2008 and 2017 are obtained by averaging Metop-A
165 and whenever Metop-B (the two instruments are considered jointly for their period of common
166 operation from March 2013 to 2017) with more than 10^5 pixels on average over the domain of
167 analysis. The number of available NH$_3$ columns depends not only on the satellite overpass time
168 but also on the state of the atmosphere being remotely sensed (e.g. thermal contrast and cloud
169 cover). IASI NH$_3$ has been evaluated using the LOTOS-EUROS model over Europe [Van Damme et
170 al., 2014b] and ground-based and airborne measurements [Van Damme et al., 2015b], showing
171 consistency between the IASI NH$_3$ and the available datasets. When comparing IASI NH$_3$
172 (previous IASI-NN version) with ground-based Fourier transform infrared (FTIR) observations, a
173 correlation of 0.8 and a slope of 0.73, with a mean relative difference of −32.4 ± (56.3)% have
174 been found [Dammers et al., 2016].

2.2.2. Cross-track Infrared Sounder (CrIS)

176 The CrIS instrument [Zavyalov et al., 2013] is a Fourier Transform spectrometer operated by the
177 Joint Polar Satellite System (JPSS) program on Suomi National Polar-orbiting Partnership (NPP)
178 satellite, launched on 28 October 2011. CrIS is in a sun-synchronous orbit with a mean local
179 daytime overpass time of 13:30 (01:30) in the ascending (descending) node. CrIS measures the
180 atmospheric composition over three wavelength bands in the infrared region (645–1095 cm^{-1};
181 1210–1750 cm^{-1}; 2155–2550 cm^{-1}). NH$_3$ retrievals are performed from the 645–1095 cm^{-1} band
182 with a spectral resolution of 0.625 cm^{-1}. The CrIS instrument scans a 2200 km swath width (+/-
183 50 °). At nadir, the CrIS field of view consists of a 3 × 3 array of circular pixels of 14 km diameter
184 each.

185 The CrIS Fast Physical Retrieval (CRPR) [Shephard and Cady-Pereira., 2015] uses an optimal
186 estimation approach [Rodgers, 2000] that minimizes the difference between the CrIS measured

Atmospheric
Chemistry
and Physics
Discussions

187 atmospheric spectra and a very fast Optimal Spectral Sampling (OSS) [Moncet et al., 2008]
188 forward model simulated spectrum to retrieve atmospheric profiles of ammonia volume mixing
189 ratios. This physical approach provides direct estimates of the retrieval errors and the vertical
190 sensitivity (averaging kernels) of the satellite observations, which is important as they vary from
191 profile-to-profile depending on the atmospheric state. The retrieved error covariance and
192 averaging kernels are also beneficial for air quality model comparisons and data assimilation
193 into models as any *a priori* information used in the retrieval can be accounted for in a robust
194 manner (i.e. observation operator). CrIS has been shown to retrieve ammonia surface
195 concentrations values down to ~0.2-0.3 ppbv under favorable conditions [Kharol, et al., 2018].
196 CrIS comparisons with ground-based FTIR observations show a correlation of 0.77 with a low
197 CrIS bias of +2% in the total column [Dammers et al., 2017]. Initial evaluation against surface
198 observations from the Ammonia Monitoring Network (AMoN) show that even with the inherent
199 sampling differences between the two surface observations they compare well with a
200 correlation of 0.76 and an overall mean CrIS – AMoN difference of ~+15% [Kharol et al., 2018].

201 For this study, the CrIS quality flag = 4 has been used, ensuring that retrievals provide some
202 information from the measurement (degrees-of-freedom- of-signal > 0.1). In addition, outliers
203 for which concentrations exceed 10 standard deviations above the mean have been removed.

204 ## 2.3. Modelling NH_3 from the CHIMERE model

205 The CHIMERE runs used in this study were obtained in the framework of the Copernicus
206 Atmospheric Monitoring Service (CAMS, https://atmosphere.copernicus.eu/), and its annual
207 task devoted to the production of regional reanalysis over Europe. The hindcasts for year 2014
208 and 2015 (raw simulation without data assimilation) were produced over Europe with a
209 horizontal   resolution   of   0.1°   per   0.1°   and
210 9 vertical levels stretched from the surface up to 500 hPa (~5000m). The input data to feed
211 CHIMERE [Menut et al., 2013; Mailler et al., 2017] were the Integrated Forecasting System (IFS)
212 meteorological data from European Centre for Medium-Range Weather Forecasts (ECMWF), the
213 annual emission inventory provided by the Netherlands Organisation for Applied Scientific
214 Research (TNO) [Kuenen et al., 2014] for year 2011 and the fire emissions from the Global Fire
215 Assimilation System (GFAS, [Kaiser et al., 2012]).The model computes hourly concentrations for
216 more than 180 species, among which are the regulated pollutants such as ozone, PM_{10}, and
217 NH_3. Within CHIMERE a comprehensive modelling system allows to compute the evolutions of
218 gaseous species and aerosols taking into account physical and chemical process. More than 30
219 gaseous species are involved in the chemical scheme and an aerosol module assesses the gas-
220 particulate phase equilibrium and compute the aerosol composition (inorganic, organic and
221 natural components).These datasets were evaluated over Europe for several pollutants before
222 being used for air quality studies (http://policy.atmosphere.copernicus.eu/Reports.html).

Atmospheric
Chemistry
and Physics
Discussions

223   The model NH$_3$ profiles were integrated vertically along the 9 km model layers to provide a
224   column that can be compared to that of the satellite measurements. Concretely this makes the
225   reasonable assumption that all the NH$_3$ is located within this 0-5km layer (see e.g. Figure 1 in
226   [Whitburn et al., 2016]).

227   ## 2.4.   Relative scales and coincidence criteria for dataset comparisons

228   Direct quantitative comparisons of satellite NH$_3$ products are difficult because of the different
229   overpass times and ground footprint sizes of the 2 space borne instruments, which are not
230   compatible with the high variability of NH$_3$ in space and time. Therefore, the evaluation of
231   satellite observations is often made with the use of in situ measurements performed at surface
232   and onboard aircrafts [Nowak et al., 2012; Van Damme et al., 2015b], or with ground-based
233   remote-sounding FTIR [Dammers et al., 2016; Dammers et al., 2017].

234   The purpose here of comparing CrIS and IASI is to assess qualitatively the spatiotemporal
235   patterns of the NH$_3$ sources derived from the two datasets and use these regional observations
236   to evaluate the CHIMERE model in the domain of analysis at the local time for their respective
237   overpasses: 9:30 and 13:30. CHIMERE outputs, in terms of NH$_3$ concentrations, have already
238   been compared to the IASI observations at regional scale (Europe, [Fortems-Cheiney et al.,
239   2016], and to surface measurements at local scale (Paris, [Petetin et al., 2016]), but have never
240   been evaluated against the CrIS observations.

241   One aspect that needs to be considered when comparing concentration amounts inferred from
242   infrared satellite observations is the importance of the algorithm and the a priori information
243   used in the retrieval, especially for NH$_3$ which has limited vertical information. Some differences
244   between the IASI and CrIS observations might arise due to instrument measurement differences
245   (e.g. sensitivity), difference sampling period (e.g. overpass times of morning/evening vs middle
246   of day/night), and retrieval algorithm differences, but they have both been validated and shown
247   to capture well the spatiotemporal variations in lower tropospheric ammonia. Since the purpose
248   of our study is not to quantitatively compare IASI and CrIS NH$_3$ data, but rather to use these
249   independent datasets to assess NH$_3$ sources patterns over the domain and qualitatively
250   evaluate the CHIMERE model in term of NH$_3$ concentrations and variabilities, a standardization
251   procedure was applied to their retrieved absolute NH$_3$ columns. We computed "standardized
252   columns" for each independent dataset (IASI, CrIS, and CHIMERE, separately) for 2014 and 2015
253   over the domain of study in such a way that the corresponding values have a standard deviation
254   of 1 and a mean of 0, as in [Wilks, 2011].

255   In addition, to compare CHIMERE outputs with satellite data/columns, spatial and temporal
256   coincidence criteria have been applied. To compare satellite observations, all CrIS pixels located
257   within a 25-km radius circle from the center of the IASI ground pixels have been considered

Atmospheric
Chemistry
and Physics
Discussions

258   within the same day of measurements. A spatial criterion of 25 km has been chosen because it
259   optimizes the number of pairs involved in the statistics and improves the correlations. As for the
260   comparisons between the model and the observations: all CHIMERE outputs located within the
261   same 0.15°x0.15° grid box than the satellite and within 1 hour from its measurement have been
262   selected.

263   ## 3. Results

264   ### 3.1.   NH$_3$ regional observations derived from IASI (10-years) and CrIS (5-
265   years)

266   #### 3.1.1. Seasonal variabilities

267   First the seasonal variability was investigated over the IdF area. On a monthly basis, the 10-year
268   and 5-year averaged regional NH$_3$ total column distributions derived from IASI and CrIS were
269   found to exhibit a high seasonality over the domain (Figures 2 and 3). Note that the distributions
270   in Figures 2 and 3 have been obtained by averaging satellite NH$_3$ observations in 0.25°x 0.25°
271   grid boxes. Both satellite datasets exhibits the same variability over the domain even if the time
272   period is different (10-years versus 5-years) and the sampling hour differs (~9.30 versus ~13.30).
273   One note that CrIS and IASI NH$_3$ columns present small differences in term of NH$_3$ total columns
274   in low concentration regimes in the domain of study.

275   In these figures (2 and 3) high NH$_3$ concentrations (up to 2.10^{16} molecules/cm^2) can be observed
276   from March to August at different locations of the domain:

277   • The French Champagne-Ardennes region in March and April (Figures 2 and 3, box A),
278   • The northern part of the domain corresponding to the Netherlands and the North of Belgium
279   from April to August (Figures 2 and 3, box B), and
280   • The Brittany/Pays de la Loire regions (West of France) mainly in April and August but still
281   persistent from March to August (Figures 2 and 3, box C).

282   The observed seasonality is related to agricultural practices (fertilizer application period varying
283   as function of the crop types and farming species) and changes in temperatures, with higher
284   temperatures favoring volatilization. This explains the high concentration in July and August.

285   In the Champagne-Ardennes region, areas of hotspots do not correspond to vineyards but to
286   field vegetables and root crops (from the Institut National de la Recherche Agronomique INRA
287   https://odr.inra.fr/intranet/carto/cartowiki/index.php/OTEX_et_Orientation_Agricole_des_terri
288   toires,   and   AGRESTE,   Service   Central   d'Enquêtes   et   d'Études   Statistiques,   2015
289   http://agreste.agriculture.gouv.fr/IMG/pdf/R4215A15.pdf). This is a leader region for mineral
290   fertilization used for sugar industry in France [Ramanantenasoa et al., 2018]. Hamaoui-Laguel et
291   al. (2014) and Fortems-Cheiney et al. (2016) have previously noted that NH$_3$ emissions in this

Atmospheric
Chemistry
and Physics
Discussions

292   region, mainly due to fertilizer over barley, sugar beet, and potato starch in early March, were
293   higher than what have been reported in the EMEP inventory.

294   NH_3 concentrations are high from April to August in the northern part of the domain that is
295   known for its animal farming (Eurostat 2014, http://ec.europa.eu/eurostat/statistics-
296   explained/index.php?title=File:Livestock_density_by_NUTS_2_regions,_EU-28,_2013.png,   [Van
297   Damme et al., 2014a]).

298   In the Pays de la Loire, NH_3 concentrations are high in April and August and remain relatively
299   high from March to September. Hotspots are found in areas of livestock farming, mainly poultry
300   and granivorous, which explains the high and relatively constant NH_3 concentrations over
301   warmer periods in this region.

302   ### 3.1.2. Inter-annual variabilities

303   As can be seen in Figures 2 and 3, NH_3 concentrations are enhanced between March and August
304   in the domain. In this section, inter-annual variabilities are discussed regarding meteorological
305   conditions and agricultural practices during this time period.

306   Inter-annual variability of NH_3 is higher in springtime than in summer, e.g. in June the variance is
307   8 times lower than for the other months. To illustrate the inter-annual variability in springtime,
308   maps of monthly mean NH_3 total columns derived in March-April period from IASI (2008-2017
309   time period) and from CrIS (2013-2017 time period) are shown in Figure 4. Both satellite
310   distributions exhibit the same inter-annual variability from 2013 to 2017 with higher NH_3
311   concentrations in 2015 over the northern part of the domain than the other years. NH_3
312   concentrations derived from IASI in 2011 are 150% higher in spring (March and April) compared
313   to 2016 (Figure 4). This inter-annual variability is partly driven by meteorological conditions and
314   specific agricultural constrains (crop type and phenological stage for instance).

315   To investigate the impact of meteorological conditions on atmospheric NH_3 variability, we
316   computed the monthly mean anomalies of total precipitation versus skin temperature derived
317   from ECMWF ERA-interim [Dee et al., 2011], color coded by NH_3 total columns anomalies
318   derived from IASI, as shown in Figure 5. Monthly mean anomalies have been calculated relative
319   to the 10-years averages (in %). In this figure, monthly NH_3 total columns are at least 10% higher
320   (positive anomalies, red dots) when skin temperatures are higher and total precipitation are
321   lower than the 10-year average. In contrast, negative monthly NH_3 total columns anomalies
322   (blue dots, Figure 5) are associated with higher total precipitation and lower skin temperatures
323   than the 10-years average. To further detail this analysis, Figure 1 of the supplement
324   information shows bar plots of monthly mean NH_3 total columns derived from IASI, total
325   precipitation and skin temperature derived from ECMWF from March to August, plotted in
326   different colors for the different years of measurements from 2008 to 2017. NH_3 total columns

Atmospheric
Chemistry
and Physics
Discussions

327   are larger by more than 300% in March-April 2012 compared to 2013 (Figure S1a). Total
328   precipitation is higher (0.4 mm compared to 1 mm, Figure S1b) and skin temperature is lower
329   (281 compared to 288 K, Figure S1c) in March 2013 than in March 2012 on average over the
330   domain. Overall, total precipitation is anti-correlated with NH_3 concentrations in the
331   atmosphere (R = -0.52 from March to August for all years, not shown here) because of a) the
332   wet deposition importance in the atmospheric NH_3 removal and b) the absence of fertilization
333   during rainy periods. Skin temperature is relatively correlated with NH_3 concentrations (R = 0.33
334   from March to August for all years) since higher temperature increases volatilization of NH_3
335   from the surface to the atmosphere.

336   In addition, NH_3 concentration is maximum in March 2011 whereas it peaks later in April for
337   2012 (Figure S1a). Springtime is a spreading fertilizer period depending on many agricultural and
338   meteorological constrains. When temperature are mild, such as in 2012 (Figure S1b), fertilizer
339   spreading occurs sooner because the phenological growth stage is more advanced. Fertilizing
340   process period also varies in function of the sowing date which depends on agricultural
341   practices and crop types: corn is fertilized in early spring whereas rapeseed is in late spring.

342   Overall, all these meteorological (precipitation and temperature) and agricultural (fertilizer and
343   manure applications) parameters account for the high NH_3 inter-annual variabilities revealed by
344   both IASI and CrIS in the domain of study.

3.2.   Comparisons of NH_3 columns derived from IASI, CrIS, and CHIMERE for 2014 and 2015

347   To discuss the representation of agricultural emissions in the models in terms of intensity and
348   both spatial and temporal distributions, regional satellite observations derived from IASI and
349   CrIS have been compared to the CHIMERE model in the region of analysis.

3.2.1. Annual cycle

351   Standardized monthly mean concentrations derived from IASI, CrIS, and CHIMERE for 2014 and
352   2015 are shown in Figure 6. These years were selected as NH_3 total columns were found to vary
353   a lot, reaching 10% higher in March and 50% lower in May than the 10-years average

354   As can be seen from the plot, the 3 datasets exhibit similar patterns in terms of seasonality: all
355   are enhanced in March-April and in summer, and show a decrease in May. However two major
356   differences can be noted. First, CrIS standardized NH_3 columns are higher in winter (November,
357   December, and January) compared to the other dataset which can be also be seen in Figure 3.
358   This could be attributed to a higher number of outliers, given the larger standard deviation
359   (shaded areas, Figure 6) and no attempt to account for potential non-detects when
360   concentrations fall below the instrument detection limits. For these months, NH_3 levels are low

Atmospheric
Chemistry
and Physics
Discussions

361   and undetectable by satellite observations (Figures 2 and 3) so these high values could be

362   interpreted as observational noise. The detection limit depends on the instrument

363   characteristics and atmospheric state, with IASI minimum detection limit of ~2-3 ppbv (~4-6.10^{15}

364   molecules.cm^{-2}) [Clarisse et al., 2010] and CrIS ~0.5-1.0 ppbv (~1-2.10^{15} molecules.cm^{-2})

365   [Shephard and Cady-Pereira, 2015; Kharol et. al., 2018]. Second, the CHIMERE standardized NH$_3$

366   columns are enhanced in September 2014, which is not supported by the observations. It has

367   been recently shown that CHIMERE overestimated NH$_3$ emissions in autumn over Europe

368   [Couvidat et al., 2018]. Generally, the amplitude of the modelled seasonal cycle exceeds the

369   measured ones, which could be explained by higher concentrations measured in winter due to

370   the observational noise and lower emissions.

371   Over the whole period, the coefficient of determination (r^2) between the standardized monthly

372   mean NH$_3$ columns derived from IASI (CrIS), and the CHIMERE model is 0.58 (0.18) for the

373   annual cycles of 2014 and 2015 (not shown here). If we only consider months of high NH$_3$ in the

374   domain from March to August, the correlation between the observational datasets and the

375   model is good with linear regression slope values between IASI (CrIS) and CHIMERE of 0.98

376   (0.71), as shown in Figure 7. The seasonal cycle is thus well reproduced by the model, which is

377   encouraging given the fact that annual total emissions are simply disaggregated with a monthly

378   profile in the model. However, the values of the r^2 lower than 0.5 indicate that the CHIMERE

379   model only reproduces at most half of the observed monthly temporal NH$_3$ variabilities in the

380   domain. Similar variabilities are found between the observations and the model outputs since

381   the coefficients of correlation of the standard deviations are 0.4 and 0.6 between CHIMERE and

382   IASI and CrIS, respectively.

383   3.2.2. Spatial variability of NH$_3$ in springtime

384   The IASI and CrIS regional maps have been compared to the CHIMERE model for the March-April

385   period in 2014 and 2015 to evaluate the model's capacity to reproduce the spatial distribution

386   of the episodic emissions from fertilizer spreading practices in springtime, as well as their inter-

387   annual variability. Satellite NH$_3$ measurements in springtime have been gridded at 0.15°x 0.15°

388   spatial resolution, and the associated CHIMERE maps have been computed following the

389   coincident criteria described in section 2.4 at the same spatial resolution (Figures 8 and 9).

390   First one can notice that the spatial distribution of NH$_3$ observed in springtime by both satellite

391   instruments are in good agreement, even though their overpass time is different (~4 hours

392   apart). This was already seen in the inter-annual variability agreement seen in Figure 4. In spring

393   2014, IASI and CrIS both reveal three main regions of enhanced NH$_3$ concentrations (North,

394   Champagne-Ardennes, and Brittany/Pays de la Loire region) already identified by the 10-years

395   and 5-years of IASI and CrIS observation maps (Boxes A, B, and C of Figures 2 and 3). In 2015,

396   concentrations of NH$_3$ in the northern part of the domain are higher than in 2014, as indicated

Atmospheric
Chemistry
and Physics
Discussions

397 by both IASI and CrIS observations (Figure 9, upper panels). Overall, satellite observations are

398 able to capture similar spatial distributions of high NH_3 concentrations in springtime, and their

399 evolution in time.

400 In spring 2014, the CHIMERE model reproduces the high concentrations in the three regions of

401 the domain identified in Figures 2 and 3. Additional NH_3 hot spots in the southeastern part of

402 the domain including the Po Valley, Switzerland, and the wine region between Besancon and

403 Lyon (blue box in Figure 8) are indicated by the CHIMERE model. NH_3 emissions in this latter

404 region are comparable to average agricultural plains over France. Only dispersion conditions

405 related to wind speed and boundary layer height can explain high NH_3 concentrations over this

406 area.

407 In spring 2015, satellite observations and the CHIMERE model outputs exhibit very similar

408 patterns in term of high NH_3 distributions, with however higher NH_3 concentrations indicated by

409 the model in the southern part of the domain (blue box in Figure 9).

410 Finally, the (model - observations) differences between the standardized NH_3 column derived

411 from the satellite instruments in springtime 2014-2015 and the corresponding NH_3 columns

412 derived from the CHIMERE model are shown in Figure 2 of the supplement information. One

413 can see that very similar patterns are presented when comparing the model to independent

414 satellite observations from IASI and CrIS: the modelled NH_3 concentrations are systematically

415 lower for both years over Belgium and United Kingdom, and higher in the southern part of the

416 domain (green square, Figure S2) including the Pays de la Loire region (box C in Figures 2 and 3),

417 and in the southeastern part of the domain (over the North part of Switzerland and the Plateau

418 du Jura region - between Besancon and Lyon cities – blue box in Figure 8). Reasons of enhanced

419 NH_3 columns derived from the model in this latter region are not clear yet. An explanation could

420 be that the temporal distribution of the emissions is misrepresented in the model since the

421 modelled concentrations are enhanced in April whereas the two satellite observations are

422 enhanced earlier in March for both years. It is worth noting that there are no EMEP stations

423 measuring surface NH_3 concentrations in these regions. As for the Brittany/Pays de la Loire

424 region, it has already been shown that the LOTOS-EUROS atmospheric model [Schaap et al.,

425 2008] using similar chemistry schemes and NH_3 emissions shows higher columns each year in

426 this area [Van Damme et al., 2014b].

427 ### 3.3. Conditions for PM formation in the Paris megacity

428 To investigate the impact of intensive agriculture practices on the Paris megacity air quality, we

429 need to better understand the role of NH_3 in the formation of $PM_{2.5}$ that depends, among

430 others, on specific meteorological conditions such as atmospheric temperature and humidity

431 that alter the gas-particle partitioning. The link between high NH_3 concentrations inducing $PM_{2.5}$

Atmospheric
Chemistry
and Physics
Discussions

432   formation in the Paris megacity is known [Petetin et al., 2016; Zhang et al., 2013] but
433   quantification of such phenomena is difficult due the lack of long-term NH_3 monitoring in the
434   IdF region. $PM_{2.5}$ is however measured hourly at several locations in Paris by the Airparif
435   network (https://www.airparif.asso.fr/, Figure 1). Thanks to the 10 years of IASI observations,
436   an observational evidence of $PM_{2.5}$ formation in the IdF region (100 km around Paris - black box
437   in Figure 1) is represented in Figure S3. Simultaneous enhancements in March of $PM_{2.5}$
438   measured at the surface and NH_3 columns derived from the IASI observations over the IdF
439   region are clearly visible. However, high concentrations of NH_3 observed in summer are not
440   associated with high $PM_{2.5}$ concentrations. This reflects the complexity of the $PM_{2.5}$ formation
441   depending on various factors, such as NH_3 emissions, atmospheric chemistry (acidic content of
442   the atmosphere), transport, and specific meteorological conditions involved in the gas to solid
443   phase conversion between NH_3 and ammonium salts.

444   To evaluate the impact of long-range transport on NH_3 levels observed over the Parisian region
445   (IdF) in spring, back-trajectory analysis was performed. In total 231 24-hours back-trajectories
446   ending in Paris (period from February 15th to May 15th from 2013 to 2016) were classified into 8
447   clusters using HYSPLIT (https://ready.arl.noaa.gov/HYSPLIT.php). Figure 10 shows the mean
448   trajectories for each cluster associated with the average NH_3 total columns measured by IASI
449   over the IdF region. In this figure, higher NH_3 columns are found under the influence of air
450   masses transported from the northern part of the domain (over Belgium and the Netherlands,
451   clusters 4 and 5) and from the Brittany region (cluster 8), which are the major sources regions of
452   NH_3 in spring in the domain as previously identified (Figures 2 and 3). Clusters 2 and 3 (Figure
453   10) are associated with intermediate NH_3 levels since air masses moved slowly transporting
454   NH_3-rich air from rural regions near IdF (such as the Champagne-Ardennes region - Box A in
455   Figures 2 and 3) to Paris. Finally, low NH_3 concentrations are measured when air masses
456   originated from ocean regions passing through continental areas with minor NH_3 sources in
457   spring (clusters 1, 6 and 7, Figure 10). This reflects the importance of long-range transport in the
458   NH_3 budget observed over the Paris megacity in spring.

459   To quantitatively assess the influence of meteorological parameters on the formation of $PM_{2.5}$
460   from NH_3 in the IdF region, timeseries of NH_3 total columns, $PM_{2.5}$ surface concentrations, and
461   four meteorological parameters (temperature at 2 m, boundary layer height, total precipitation
462   and relative humidity) derived from ECMWF - ERA-Interim [Dee et al., 2011] were analyzed. To
463   compute daily and monthly means, IASI NH_3 total columns have been averaged over IdF (black
464   box in Figure 1), $PM_{2.5}$ concentrations measured between 9 AM and 11 AM have been averaged
465   over the 14 stations (dark points in Figure 1), and ECMWF data have been averaged over a 300
466   km region around Paris (the blue box in Figure 1). Figure 11 shows all these parameters for
467   spring 2014.

Atmospheric
Chemistry
and Physics
Discussions

468   We have flagged pollution episodes in both time series (PM$_{2.5}$ and NH$_3$) by selecting data above
469   1-sigma standard deviation over the mean of the datasets from 2013 to 2016. This time period
470   was selected to have enough IASI observations in the IdF region. Then two cases have been
471   defined to study the temporal correlation between NH$_3$ and PM$_{2.5}$: case A in which both NH$_3$ and
472   PM$_{2.5}$ pollution episodes appear simultaneously, i.e. within the same day or 2 days apart
473   (shaded in red in Figure 11); case B in which pollution episodes appear at least 3 days apart
474   (shaded in blue in Figure 11). In Figure 11, a strong relationship between peaks of NH$_3$, PM$_{2.5}$
475   and meteorological parameters can be seen. For example, between March 3rd and March 19th
476   2014 (case A), the boundary layer height is exceptionally low (456 m; compared to 760 m on
477   average); the temperature is relatively low (280 K; 282 K on average); and there is no
478   precipitation (0.01 mm/h; 0.11 mm/h on average). One note that peaks of maximum NH$_3$
479   observed in IdF on March 11th and 12th are associated with air masses coming from the northern
480   part of the domain (clusters 4 and 5 in Figure 10). In contrast, for the case B in which
481   appearance of peaks of NH$_3$ and PM$_{2.5}$ is not simultaneous, meteorological conditions are
482   different: the boundary layer is thicker (908 m on April 23rd 2014), or temperature is higher (285
483   K on April 11th 2014).

484   To further investigate the influence of meteorological parameters on the pollution episodes in
485   the IdF region, detailed analysis have been made over the whole dataset. Figure 12 shows the
486   statistical distribution of meteorological parameters corresponding to case A, case B, and all
487   observations. One can see that the boundary layer height is significantly lower in case A (550 ±
488   205 m) than in case B (751 ± 276 m), and that precipitations are absent in case A (0,019 mm/h)
489   compared to case B (0,085 mm/h). The temperature at 2 meters also differs between the two
490   cases (case A: 278 ± 3 K; case B: 282 ± 4 K), but the humidity is almost the same (70% ± 17%
491   versus 75%±18%). Thus the combination of the following three meteorological parameters favors
492   simultaneous appearances of NH$_3$ and of PM$_{2.5}$ in Paris (i.e. case A): low surface temperatures
493   (5°C), with thin boundary layers (~500m), and rare precipitations. In addition, the Wilcoxon-
494   Mann-Whitney test ([Wilks, 2011], not shown here) indicates that each single parameter has no
495   significant influence on the NH$_3$-PM$_{2.5}$ correlation. Therefore only a combination of these
496   different parameters has an impact on secondary aerosol formation from NH$_3$.

497   An explanation of these findings might be that anticyclonic conditions (low planetary boundary
498   layer), preventing pollutant dispersions in the lower atmosphere [Salmond and McKendry,
499   2005], along with moderate wind fields allow NH$_3$ plumes to be transported from rural to urban
500   regions [Petit et al., 2015]. In addition, thanks to relatively low atmospheric temperatures and a
501   moderate relative humidity, conversion of gas phase NH$_3$ to ammonium salts is then
502   accentuated via optimal phase equilibrium [Watson et al., 1994; Nenes et al., 1998]. Finally,
503   with the absence of rain, ammonium salts are stabilized in the aerosols.

504   Our observations are in agreement with previous studies [Bessagnet et al., 2016; Wang et al.,
505   2015], which have shown that the formation of ammonium salt needs a specific humidity of 60 -
506   70%, because it corresponds to the deliquescence point of NH_4NO_3 in ambient air. This is in
507   agreement with our results since the mean of relative humidity in case A is 70%. Our results also
508   support the idea that a relatively low atmospheric temperature favor $PM_{2.5}$ formation since the
509   phase equilibrium leads to NH_4NO_3 decomposition above 30 °C.

4. Conclusions

511   This study focuses on seasonal and inter-annual variabilities of NH_3 concentrations in a 400 km
512   radius-circle area around Paris to assess the evolution of major NH_3 agricultural sources and its
513   key role in the formation of the secondary aerosols that affect air quality over the Paris
514   megacity.

515   Thanks to 10-years and 5-years of regional NH_3 observations derived from IASI and CrIS, three
516   main regions of high NH_3 occurring between March and August were identified. Observed inter-
517   annual variabilities of NH_3 concentrations have been discussed with respect to total
518   precipitations and atmospheric temperature, showing that total precipitations are anti-
519   correlated with high NH_3 concentrations, and that mild temperature in late winter causes
520   precocious fertilizer spreading due to advanced phenological growth stage.

521   To evaluate our knowledge on agricultural emissions in terms of intensity and both spatial and
522   temporal distributions, coincident CHIMERE model outputs have been compared to satellite
523   observations of IASI and CrIS for 2014 and 2015. The annual cycle is well reproduced by the
524   model (correlation slopes of 0.98 and 0.71 between the model and IASI and CrIS, respectively)
525   but the model is only able to reproduce half of the observed atmospheric NH_3 variability.
526   Focusing on spring periods (March-April 2014 and 2015) of episodic NH_3 emissions, the two
527   independent satellite observations derived from IASI and CrIS show very similar spatial
528   distributions of high NH_3 concentrations, as well as their evolution in time. The comparison
529   between CHIMERE NH_3 columns and coincident satellite observations highlights the same
530   difference spatial patterns with a systematic underestimation of NH_3 concentrations from the
531   model over Belgium and an overestimation in the southern part of the domain (French
532   Brittany/Pays de la Loire and Plateau du Jura regions, as well as North of Switzerland).

533   Focusing on the Ile-de-France (IdF, 100 km around Paris) region, we found that air masses
534   originated from rich-NH_3 areas, mainly the northern part of the domain over Belgium and the
535   Netherlands, increase the observed NH_3 total columns measured by IASI over the urban area of
536   Paris.

537   To assess the link between NH_3 and $PM_{2.5}$ over the Parisian (IdF) region, the main
538   meteorological parameters driving the optimal conditions involved in the $PM_{2.5}$ formation have

Atmospheric
Chemistry
and Physics
Discussions

Open Access

EGU

539   been identified. The results show that relatively low temperature, thin boundary layer, coupled
540   with almost no precipitation, favor the PM$_{2.5}$ formation with the presence of atmospheric NH$_3$ in
541   the IdF region. Based on a more observational approach over large time scale, this work is in
542   agreement with previous studies.

543   This study highlights the need for a better representative NH$_3$ monitoring to improve numerical
544   simulation of spatial and temporal NH$_3$ variabilities, especially at fine scales. In order to
545   compare IASI and CrIS data in absolute values, it would be recommended to derive both
546   datasets using the same retrieval algorithm. Thus, by combining these datasets bi-daily NH$_3$
547   total columns in absolute values at regional scale would be provided. This would help inferring
548   variability of top-down NH$_3$ emissions. Complementarily, long term quantification of NH$_3$ diurnal
549   cycle inside Paris would improve comparisons with local PM$_{2.5}$ needed to understand secondary
550   aerosols formations. For this purpose, an ongoing activity consists in the deployment of a mini-
551   DOAS instrument [Volten et al., 2012] used for long-term and continuous monitoring of
552   atmospheric NH$_3$ concentrations in the center of Paris from the QUALAIR platform
553   (https://www.ipsl.fr/en/Our-research/Atmospheric-chemistry-and-air-quality/Tropospheric-
554   chemistry/QUALAIR). Finally, the geostationary-orbit sounder IRS-MTG ([Stuhlmann et al.,
555   2005], to be launched after 2022) will provide NH$_3$ columns at very high sampling rate (every 0.5
556   hour over Europe) with an unpreceded spatial resolution (pixel size of 4 km).

Author contribution:
559   CV wrote the paper with contributions of all coauthors. CV and CC designed the study. MV, LC,
560   and SW performed IASI retrievals and ED, MWS, and KEC performed the CrIS retrievals. FM ran
561   the CHIMERE simulations. CV and TW analyzed the data with guidance from CC and PFC. All
562   authors discussed the results and contributed to the final paper.

Acknowledgement:

Atmospheric
Chemistry
and Physics
Discussions

576   Engineering Center (SSEC) and the NOAA Comprehensive Large Array-Data Stewardship System

577   (CLASS) (Liu et al.,2014), with special thanks to Axel Graumann (NOAA).

578

579   <u>References</u>

580   Battye, W., Aneja, V. P., and Schlesinger W. H.: Is nitrogen the next carbon?, Earth's Future, 5,

581   894–904, doi:10.1002/2017EF000592, 2017.

582   Beer, R., Shephard, M. W., Kulawik, S. S., Clough, S. A., Eldering, A., Bowman, K. W., Sander, S.

583   P., Fisher, B. M., Payne, V. H., Luo, M., Osterman, G. B., and Worden, J. R.: First satellite

584   observations of lower tropospheric ammonia and methanol, Geophys. Res. Lett., 35, L09801,

585   doi:10.1029/2008GL033642, 2008.

586   Behera, S. N., Sharma, M., Aneja, V. P., and Balasubramanian, R.: Ammonia in the atmosphere: a

587   revieon emission sources, atmospheric chemistry and deposition on terrestrial bodies, Environ.

588   Sci. Pollut. Res. Int., 20, 8092-8131, doi: 10.1007/s11356-013-2051-9, 2013.

589   Bessagnet, B., Meleux, F., Favez, O., Beauchamp, M., Colette, A., Couvidat, F., Rouïl, L., Menut,

590   L. : Le rôle de l'agriculture sur les concentrations en particules dans l'atmosphère et l'apport de

591   la modélisation (the role of agriculture on the concentrations of particles in the atmosphere and

592   supply modeling), Pollution atmosphérique, climat, santé, société, 229–230, 154–165, 2016.

593   Bey, I., Jacob, D. J., Yantosca, R. M., Logan, J. A., Field, B., Fiore, A. M., Li, Q., Liu, H., Mickley, L.

594   J., and Schultz, M.: Global modeling of tropospheric chemistry with assimilated meteorology:

595   Model description and evaluation, J. Geophys. Res., 106, 23,073-23,096, 2001.

596   Clerbaux, C., Boynard, A., Clarisse, L., George, M., Hadji-Lazaro, J., Herbin, H., Hurtmans, D.,

597   Pommier, M., Razavi, A., Turquety, S., Wespes, C., and Coheur, P.-F.: Monitoring of atmospheric

598   composition using the thermal infrared IASI/MetOp sounder, Atmos. Chem. Phys., 9, 6041–

599   6054, doi:10.5194/acp-9-6041-2009,2009

600   CEIP, Centre on Emission Inventories and Projections, 'EMEP officially reported emission data',

601   http://www.ceip.at/ms/ceip_home1/ceip_home/webdab_emepdatabase/reported_emissionda

602   ta/, last access July 2018.

603   CITEPA, Centre Interprofessionnel Technique d'Etudes de la Pollution Atmosphérique, Format

604   SECTEN, https://www.citepa.org/fr/air-et-climat/polluants/aep-item/ammoniac, last access

605   April 2018.

606 Clarisse, L., Clerbaux, C., Dentener, F., Hurtmans, D., and Coheur, P.-F.: Global ammonia
607 distribution derived from infrared satellite observations, Nat. Geosci., 2, 479–483,
608 https://doi.org/10.1038/ngeo551, 2009.

609 Clarisse, L., Shephard, M., Dentener, F., Hurtmans, D., Cady-Pereira, K., Karagulian, F., Van
610 Damme, M., Clerbaux, C., and Coheur, P.-F.: Satellite monitoring of ammonia: A case study of
611 the San Joaquin Valley, J. Geophys. Res., 115, D13302, https://doi.org/10.1029/2009JD013291,
612 2010.

613 Couvidat, F., Bessagnet, B., Garcia-Vivanco, M., Real, E., Menut, L., and Colette, A.: Development
614 of an inorganic and organic aerosol model (CHIMERE 2017β v1.0): seasonal and spatial
615 evaluation over Europe, Geosci. Model Dev., 11, 165-194, https://doi.org/10.5194/gmd-11-165-
616 2018, 2018.

617 Corso, M. Medina, S., and Tillier, C. : Quelle est la part des pics de pollution dans les effets à
618 court terme de la pollution de l'air sur la santé dans les villes de France ? Saint-Maurice: Santé
619 publique France, ISBN : 979-10-289-0259-9, 2016.

620 Dammers, E., Palm, M., Van Damme, M., Vigouroux, C., Smale, D., Conway, S., Toon, G. C.,
621 Jones, N., Nussbaumer, E., Warneke, T., Petri, C., Clarisse, L., Clerbaux, C., Hermans, C., Lutsch,
622 E., Strong, K., Hannigan, J. W., Nakajima, H., Morino, I., Herrera, B., Stremme, W., Grutter, M.,
623 Schaap, M., Wichink Kruit, R. J., Notholt, J., Coheur, P.-F., and Erisman, J. W.: An evaluation of
624 IASI-NH3 with ground-based Fourier transform infrared spectroscopy measurements, Atmos.
625 Chem. Phys., 16, 10351–10368, https://doi.org/10.5194/acp-16-10351-2016, 2016.

626 Dammers, E., Shephard, M. W., Palm, M., Cady-Pereira, K., Capps, S., Lutsch, E., Strong, K.,
627 Hannigan, J. W., Ortega, I., Toon, G. C., Stremme, W., Grutter, M., Jones, N., Smale, D., Siemons,
628 J., Hrpcek, K., Tremblay, D., Schaap, M., Notholt, J., and Erisman, J. W.: Validation of the CrIS fast
629 physical NH3 retrieval with ground-based FTIR, Atmos Meas Tech, 10, 2645-2667, 10.5194/amt-
630 10-2645-2017, 2017.

631 Dee, D. P., Uppala, S. M., Simmons, A. J., Berrisford, P., Poli, P., Kobayashi, S., Andrae, U.,
632 Balmaseda, M. A., Balsamo, G., Bauer, P., Bechtold, P., Beljaars, A. C. M., van de Berg, L., Bidlot,
633 J., Bormann, N., Delsol, C., Dragani, R., Fuentes, M., Geer, A. J., Haimberger, L., Healy, S. B.,
634 Hersbach, H., Hólm, E. V., Isaksen, L., Kållberg, P., Köhler, M., Matricardi, M., McNally, A. P.,
635 Monge-Sanz, B. M., Morcrette, J.-J., Park, B.-K., Peubey, C., de Rosnay, P., Tavolato, C., Thépaut,
636 J.-N. and Vitart, F.: The ERA-Interim reanalysis: configuration and performance of the data
637 assimilation system. Q.J.R. Meteorol. Soc., 137: 553–597. doi: 10.1002/qj.828, 2011.

638 Erisman, J. W., Sutton, M. A., Galloway, J. N., Klimont, Z., and Winiwarter, W.: How a century of
639 ammonia synthesis changed the world, Nat. Geosci., 1, 636–639, doi:10.1038/ngeo325, 2008.

Atmospheric
Chemistry
and Physics
Discussions

Open Access

EGU

640 Fortems-Cheiney, A., Dufour, G., Hamaoui-Laguel, L., Foret, G., Siour, G., Van Damme, M.,
641 Meleux, F., Coheur, P.-F., Clerbaux, C., Clarisse, L., Favez, O., Wallasch, M., and Beekmann, M.:
642 Unaccounted variability in NH3 agricultural sources detected by IASI contributing to European
643 spring haze episode, Geophys. Res. Lett., 43, 5475–5482, doi:10.1002/2016GL069361, 2016.

644 Fuzzi, S., Baltensperger, U., Carslaw, K., Decesari, S., Denier van der Gon, H., Facchini, M. C.,
645 Fowler, D., Koren, I., Langford, B., Lohmann, U., Nemitz, E., Pandis, S., Riipinen, I., Rudich, Y.,
646 Schaap, M., Slowik, J. G., Spracklen, D. V., Vignati, E., Wild, M., Williams, M., and Gilardoni, S.:
647 Particulate matter, air quality and climate: lessons learned and future needs, Atmos. Chem.
648 Phys., 15, 8217-8299, https://doi.org/10.5194/acp-15-8217-2015, 2015.

649 Galloway, J. N., Aber, J. D., Erisman, J. W., Seitzinger, S. P., Howarth, R. W., Cowling, E. B., and
650 Cosby, B. J.: The Nitrogen Cascade, BioScience, 53, doi: 10.1641/0006-3568(2003), 2003.

651 Gong, L., Lewicki, R., Griffin, R.J., Tittel, F.K., Lonsdale, C.R., Stevens, R.G., Pierce, J.R., Malloy,
652 Q.G.J., Travis, S.A., Bobmanuel, L.M., Lefer, B.L., and Flynn, J.H.: Role of atmospheric ammonia in
653 particulate matter formation in Houston during summertime, Atmos. Environ, 77: 893–900,
654 https://doi.org/10.1016/j.atmosenv.2013.04.079, 2013.

655 Hamaoui-Laguel, L., Meleux, F., Beekmann, M., Bessagnet, B., Génermont, S., Cellier, P.,
656 Létinois, L..: Improving ammonia emissions in air quality modelling for France, Atmos. Environ.,
657 92, 584–595, doi:10.1016/j.atmosenv.2012.08.002, 2014.

658 Heald, C.L., Collett Jr., J.L., Lee, T., Benedict, K.B., Schwandner, F.M., Li, Y., Clarisse, L., Hurtmans,
659 D.R., Van Damme, M., Clerbaux, C., Coheur, P.-F., Philip, S., Martin, R.V., and Pye, H.O.T.:
660 Atmospheric ammonia and particulate inorganic nitrogen over the United States, Atmos. Chem.
661 Phys., 12, 10295–10312, doi:10.5194/acp-12-10295-2012, 2012.

662 Holland, E.A., Bertman, S.B., Carroll, M.A., Guenther, A.B., Shepson, P.B., Sparks, J.P., and Lee-
663 Taylor, J.: U.S. Nitrogen Science Plan Focuses Collaborative Efforts, Eos. Trans. Am. Geophys.
664 Union., 86(27), 253-260, 2005.

665 Kaiser, J. W., Heil, A., Andreae, M. O., Benedetti, A., Chubarova, N., Jones, L., Morcrette, J.-J.,
666 Razinger, M., Schultz, M. G., Suttie, M., and van der Werf, G. R.: Biomass burning emissions
667 estimated with a global fire assimilation system based on observed fire radiative power. BG,
668 9:527-554, 2012.

669 Kharol, S. K., M. W. Shephard, C. A. McLinden, L. Zhang, C. E. Sioris, J. M. O'Brien, R. Vet, K. E.
670 Cady-Pereira, E. Hare, J. Siemons, and N. A. Krotkov.: Dry deposition of reactive nitrogen from
671 satellite observations of ammonia and nitrogen dioxide over North America, Geophysical
672 Research. Letters, 45, 1157-1166, https://doi.org/10.1002/2017GL075832, 2018.

673

674   Kranenburg, R., Hendriks, C., Kuenen, J., and Schaap, M.: Improved Modelling of Ammonia by
675   Using Manure Transport Data, In International Technical Meeting on Air Pollution Modelling and
676   its Application (pp. 483-486). Springer, Cham, December 2016.

678   Kuenen, J. J. P., Visschedijk, A. J. H., Jozwicka, M., and Denier van der Gon, H. A. C.: TNO-
679   MACC_II emission inventory; a multi-year (2003–2009) consistent high-resolution European
680   emission inventory for air quality modelling, Atmos. Chem. Phys., 14, 10963-10976,
681   https://doi.org/10.5194/acp-14-10963-2014, 2014.

683   Li, Y., Thompson, T. M., Van Damme, M., Chen, X., Benedict, K. B., Shao, Y., Day, D., Boris, A.,
684   Sullivan, A. P., Ham, J., Whitburn, S., Clarisse, L., Coheur, P.-F., and Collett Jr., J. L.: Temporal and
685   spatial variability of ammonia in urban and agricultural regions of northern Colorado, United
686   States, Atmos. Chem. Phys., 17, 6197-6213, https://doi.org/10.5194/acp-17-6197-2017, 2017.

688   Mailler, S., Menut, L., Khvorostyanov, D., Valari, M., Couvidat, F., Siour, G., Turquety, S., Briant,
689   R., Tuccella, P., Bessagnet, B., Colette, A., Letinois, L., and Meleux, F.: CHIMERE-2017: from
690   urban to hemispheric chemistry-transport modeling, Geosci. Model Dev., 10, 2397-2423,
691   https://doi.org/10.5194/gmd-10-2397-2017, 2017.

692   Menut, L., Bessagnet, B., Khvorostyanov, D., Beekmann, M., Blond, N., Colette, A., Coll, I., Curci,
693   G., Foret, G., Hodzic, A., Mailler, S., Meleux, F., Monge, J.L., Pison, I., Siour, G., Turquety, S.,
694   Valari, M., Vautard, R., and Vivanco, M.G.: CHIMERE 2013: a model for regional atmospheric
695   composition modelling, Geosci. Model Dev, 6, 981-1028, doi:10.5194/gmd-6-981-2013, 2013.

696   Moran, M. D., Dastoor, A., and Morneau, G.: Long-Range Transport of Air Pollutants and
697   Regional and Global Air Quality Modelling. In: Taylor E., McMillan A. (eds) Air Quality
698   Management, Springer, Dordrecht, 2014.

699   Moncet, J.-L, Uymin G., Lipton A. E., and Snell H. E.: Infrared radiance modeling by optimal
700   spectral sampling, J. Atmos. Sci., 65, 3917-3934, https://doi.org/10.1175/2008JAS2711.1, 2008.

701   Myhre, G., Samset, B. H., Schulz, M., Balkanski, Y., Bauer, S., Berntsen, T. K., Bian, H., Bellouin,
702   N., Chin, M., Diehl, T., Easter, R. C., Feichter, J., Ghan, S. J., Hauglustaine, D., Iversen, T., Kinne,
703   S., Kirkevåg, A., Lamarque, J.-F., Lin, G., Liu, X., Lund, M. T., Luo, G., Ma, X., van Noije, T., Penner,
704   J. E., Rasch, P. J., Ruiz, A., Seland, Ø., Skeie, R. B., Stier, P., Takemura, T., Tsigaridis, K., Wang, P.,
705   Wang, Z., Xu, L., Yu, H., Yu, F., Yoon, J.-H., Zhang, K., Zhang, H., and Zhou, C.: Radiative forcing of
706   the direct aerosol effect from AeroCom Phase II simulations, Atmos. Chem. Phys., 13, 1853-
707   1877, https://doi.org/10.5194/acp-13-1853-2013, 2013.

708   National   Emission   Ceilings   Directive   (NEC)   reporting   status,   doi:10.2800/984979,
709   https://www.eea.europa.eu/themes/air/national-emission-ceilings/nec-directive-reporting-
710   status-2018, 2018.

711   Nenes, A.; Pandis, S. N.; Pilinis, C.: ISORROPIA: A New Thermodynamic Equilibrium Model for
712   Multiphase Multicomponent Inorganic Aerosols. Aquat. Geoch., 4, 123-152, 1998.

713   Nowak, J. B., Neuman, J. A., Bahreini, R., Middlebrook, A. M., Holloway, J. S., McKeen, S. A.,
714   Parrish, D. D., Ryerson, T. B., and Trainer, M.: Ammonia sources in the California South Coast Air
715   Basin and their impact on ammonium nitrate formation, Geophys. Res. Lett., 39, L07804,
716   https://doi.org/10.1029/2012GL051197, 2012.

717   Petetin, H., Sciare, J., Bressi, M., Gros, V., Rosso, A., Sanchez, O., Sarda-Estève, R., Petit, J.-E.,
718   and Beekmann, M.: Assessing the ammonium nitrate formation regime in the Paris megacity
719   and its representation in the CHIMERE model, Atmos. Chem. Phys., 16, 10419-10440,
720   https://doi.org/10.5194/acp-16-10419-2016, 2016.

721   Petit, J.-E., Favez, O., Sciare, J., Crenn, V., Sarda-Estève, R., Bonnaire, N., Močnik, G., Dupont, J.-
722   C., Haeffelin, M., and Leoz-Garziandia, E.: Two years of near real-time chemical composition of
723   submicron aerosols in the region of Paris using an Aerosol Chemical Speciation Monitor (ACSM)
724   and   a   multi-wavelength   Aethalometer,   Atmos.   Chem.   Phys.,   15,   2985-3005,
725   https://doi.org/10.5194/acp-15-2985-2015, 2015.

726   Pinder, R. W., Adams, P. J., Pandis, S.N., and Gilliland, A. B.: Temporally resolved ammonia
727   emission inventories: current estimates, evaluation tools, and measurement needs, *J*. Geophys.
728   Res., 111, D16310, http://dx.doi.org/10.1029/2005JD006603, 2006.

729   Pope III, C. A., Ezzati M., and Dockery, D. W.: Fine-particulate air pollution and life expectancy in
730   the United States, New England J. Med., 360 (4), 376-386, 2009.

731   Ramanantenasoa, M. M. J., Gilliot, J.-M., Mignolet, C., Bedos, C., Mathias, E., Eglin, T.,
732   Makowski, D., and Génermont, S.: A new framework to estimate spatio-temporal ammonia
733   emissions due to nitrogen fertilization in France, Science of The Total Environment, 645, 205 –
734   219, https://doi.org/10.1016/j.scitotenv.2018.06.202, 2018.

735   Rockström, J., Steffen, W., Noone, K., Persson, A., Chapin Iii, F. S., Lambin, E. F., Lenton, T. M.,
736   Scheffer, M., Folke, C., Schellnhuber, H. J., Nykvist, B., de Wit, C. A., Hughes, T., van der Leeuw,
737   S., Rodhe, H., Sörlin, S., Snyder, P. K., Costanza, R., Svedin, U., Falkenmark, M., Karlberg, L.,
738   Corell, R. W., Fabry, V. J., Hansen, J., Walker, B., Liverman, D., Richardson, K., Crutzen, P., and
739   Foley, J. A.: Planetary boundaries: Exploring the safe operating space for humanity, Ecology and
740   Society, 14, 2009.

741   Rodgers, C. D.: Inverse Methods for Atmospheric Sounding: Theory and Practice, vol. 2 of Series
742   on Atmospheric, Oceanic and Planetary Physics, edited by: Taylor, F. W., World Scientific, 2000.

743   Salmond, J. A., and McKendry, I. G.: A Review of Turbulence in the Very Stable Nocturnal
744   Boundary Layer and Its Implications for Air Quality, Progress in Physical Geography, 29 (2), 171–
745   188, 2005.

746   Schaap, M., Timmermans, R., Roemer, M., Boersen, G., Builtjes, P., Sauter, F., Velders, G., and
747   Beck, J.: The LOTOS-EUROS model: Description, validation and latest developments, Int. J.
748   Environ. Pollut., 32, 270–290, doi:10.1504/IJEP.2008.017106, 2008.

749   Shephard, M.W., and Cady-Pereira, K.E.: Cross-track Infrared Sounder (CrIS) satellite
750   observations of tropospheric ammonia, Atmos. Meas. Tech., 8, 1323-1336, 2015.

751   Shephard, M. W., Cady-Pereira, K. E., Luo, M., Henze, D. K., Pinder, R. W., Walker, J. T., Rinsland,
752   C. P., Bash, J. O., Zhu, L., Payne, V. H., and Clarisse, L.: TES ammonia retrieval strategy and global
753   observations of the spatial and seasonal variability of ammonia, Atmos. Chem. Phys., 11, 10743–
754   10763, doi:10.5194/acp-11-10743-2011, 2011.

755   Skjøth, C. A., Geels, C., Berge, H., Gyldenkærne, S., Fagerli, H., Ellermann, T., Frohn, L. M.,
756   Christensen, J., Hansen, K. M., Hansen, K., and Hertel, O.: Spatial and temporal variations in
757   ammonia emissions – a freely accessible model code for Europe, Atmos. Chem. Phys., 11, 5221-
758   5236, https://doi.org/10.5194/acp-11-5221-2011, 2011.

759   Skyllakou, K., Murphy, B. N., Megaritis, A. G., Fountoukis, C., and Pandis, S. N.: Contributions of
760   local and regional sources to fine PM in the megacity of Paris, Atmos. Chem. Phys., 14, 2343-
761   2352, https://doi.org/10.5194/acp-14-2343-2014, 2014.

762   Sutton, M. A., Bleeker, A., Howard, C., Bekunda, M., Grizzetti, B., de Vries, W., van Grinsven, H.,
763   Abrol, Y., Adhya, T., BillenG. and. Davidson, E., Datta, A., Diaz, R., Erisman, J., Liu, X., Oenema,
764   O., Palm, C., Raghuram, N., Reis, S., Scholz, R., Sims, T., Westhoek, H., Zhang, F., with
765   contributions from Ayyappan, S., Bouwman, A., Bustamante, M., Fowler, D., Galloway, J., Gavito,
766   M., Garnier, J., Greenwood, S., Hellums, D., Holland, M., Hoysall, C., Jaramillo, V., Klimont, Z.,
767   Ometto, J., Pathak, H., Plocq Fichelet, V., Powlson, D., Ramakrishna, K., Roy, A., Sanders, K.,
768   Sharma, C., Singh, B., Singh, U., Yan, X., and Zhang, Y.: Our Nutrient World: The challenge to
769   produce more food and energy with less pollution. Global Overview of Nutrient Management,
770   Centre for Ecology & Hydrology on behalf of the Global Partnership on Nutrient Management
771   and the International Nitrogen Initiative, 114 pp., 2013.

772   Stuhlmann, R., Rodriguez, A., Tjemkes, S., Grandell, J., Arriaga, A., Bézy, J.-L., Aminou, D., and
773   Bensi, P.: Plans for EUMETSAT's Third Generation Meteosat (MTG) Geostationary Satellite
774   Program, Adv. Space Res., 36, 975–981, 2005.

Atmospheric
Chemistry
and Physics
Discussions
Open Access
EGU

775   Toro, R.A., Canales, M., Flocchini, R.G., Morales, R.G.E., and Leiva G, M.A.: Urban atmospheric
776   ammonia in Santiago City, Chile, Aerosol Air Qual. Res., 14: 33–44, doi:
777   10.4209/aaqr.2012.07.0189, 2014.

778   Van Damme, M., Clarisse, L., Heald, C. L., Hurtmans, D., Ngadi, Y., Clerbaux, C., Dolman, A. J.,
779   Erisman, J. W., and Coheur, P. F.: Global distributions, time series and error characterization of
780   atmospheric ammonia (NH3) from IASI satellite observations, Atmos. Chem. Phys., 14, 2905–
781   2922, https://doi.org/10.5194/acp-14-2905-2014, 2014a.

782   Van Damme, M., Wichink Kruit, R. J., Schaap, M., Clarisse, L., Clerbaux, C., Coheur, P.-F.,
783   Dammers, E., Dolman, A. J., and Erisman, J. W.: Evaluating four years of atmospheric ammonia
784   (NH$_3$) over Europe using IASI satellite observations and LOTOS-EUROS model results, J. Geophys.
785   Res.-Atmos., 119, 9549-9566, 2014b.

786   Van Damme, M., Erisman, J. W., Clarisse, L., Dammers, E., Whitburn, S., Clerbaux, C., Dolman, A.
787   J., and Coheur, P.-F.: Worldwide spatiotemporal atmospheric ammonia (NH$_3$) columns variability
788   revealed by satellite, Geophys. Res. Lett., 42 (20), 8660-8668, 2015a.

789   Van Damme, M., Clarisse, L., Dammers, E., Liu, X., Nowak, J. B., Clerbaux, C., Flechard, C. R.,
790   Galy-Lacaux, C., Xu, W., Neuman, J. A., Tang, Y. S., Sutton, M. A., Erisman, J. W., and Coheur, P.
791   F.: Towards validation of ammonia (NH$_3$) measurements from the IASI satellite, Atmos. Meas.
792   Tech., 8, 1575-1591, https://doi.org/10.5194/amt-8-1575-2015, 2015b.

793   Van Damme, M., Whitburn, S., Clarisse, L., Clerbaux, C., Hurtmans, D., and Coheur, P.-F.: Version
794   2 of the IASI NH$_3$ neural network retrieval algorithm: near-real-time and reanalysed datasets,
795   Atmos. Meas. Tech., 10, 4905-4914, https://doi.org/10.5194/amt-10-4905-2017, 2017.

796   Van Damme, M., Clarisse, L., Whitburn, S., Hadji-Lazaro J., Hurtmans, D., Clerbaux, C., and
797   Coheur, P.-F.: Industrial and agricultural ammonia point sources exposed, Nature, 564 (7734):
798   99, DOI: 10.1038/s41586-018-0747-1, 2018.

799   van Vuuren, D. P., Edmonds, J., Kainuma, M. et al. he Representative Concentration Pathways:
800   An overview, Clim. Change, 109 (1–2), 5–31, https://doi.org/10.1007/s10584-011-0148-z, 2011.

801   Volten, H., Bergwerff, J. B., Haaima, M., Lolkema, D. E., Berkhout, A. J. C., van der Hoff, G. R.,
802   Potma, C. J. M., Wichink Kruit, R. J., van Pul, W. A. J., and Swart, D. P. J.: Two instruments based
803   on differential optical absorption spectroscopy (DOAS) to measure accurate ammonia
804   concentrations in the atmosphere, Atmos. Meas. Tech., 5, 413-427,
805   https://doi.org/10.5194/amt-5-413-2012, 2012.

Atmospheric
Chemistry
and Physics
Discussions
Open Access
EGU

806   Wang, S., Nan, J., Shi, C., Fu, Q., Gao, G., Wang, D., Cui, H., Saiz-Lopez A., and Zhou,B.:
807   Atmospheric ammonia and its impacts on regional air quality over the megacity of Shanghai,
808   China, Scientific Reports, 5, 15842, http://dx.doi.org/10.1038/srep15842, 2015.

809   Warner, J. X., Dickerson, R. R., Wei, Z., Strow, L. L., Wang, Y., and Liang, Q.: Increased
810   atmospheric ammonia over the world's major agricultural areas detected from space, Geophys.
811   Res. Lett., doi: 10.1002/2016gl072305, 2017.

812   Warner, J. X., Wei, Z., Strow, L. L., Dickerson, R. R., and Nowak, J. B.: The global tropospheric
813   ammonia distribution as seen in the 13-year AIRS measurement record, Atmos. Chem. Phys., 16,
814   5467-5479, https://doi.org/10.5194/acp-16-5467-2016, 2016.

815   Watson, J. G., Chow, J. C., Lurmann, F. W., and Musarra, S. P.: Ammonium Nitrate, Nitric Acid,
816   and Ammonia Equilibrium in Wintertime Phoenix, Arizona. Air & Waste, 44 (4), 405–412, 1994.

817   Whitburn, S., Van Damme, M., Clarisse, L., Bauduin, S., Heald, C., Hadji-Lazaro, J., Hurtmans, D.,
818   Zondlo, M., Clerbaux, C., and Coheur, P.-F.: A flexible and robust neural network IASI-NH3
819   retrieval   algorithm,   J.   Geophys.   Res.   Atmos.,   121,   6581–6599,
820   https://doi.org/10.1002/2016JD024828, 2016.

821   Wilks, Daniel S.: Statistical Methods in the Atmospheric Sciences, 3rd ed. Oxford, Waltham, MA:
822   Academic Press, 2011.

823   Ye, X., Ma, Z., Zhang, J., Du, H., Chen, J., Chen, H., Yang, X., Gao, W. and Geng, F.: Important role
824   of ammonia on haze formation in Shanghai, Environ. Res. Lett., 6: 024019, doi:10.1088/1748-
825   9326/6/2/024019, 2011.

826   Zavyalov, V., Esplin, M., Scott, D., Esplin, B., Bingham, G., Hoffman, E., Lietzke, C., Predina, J.,
827   Frain, R., Suwinski, L., Han, Y., Major, C., Graham, B., and Phillips, L.: Noise performance of the
828   CrIS instrument, J. Geophys. Res., doi: 10.1002/2013JD020457, 2013.

829   Zhang, Q. J., Beekmann, M., Drewnick, F., Freutel, F., Schneider, J., Crippa, M., Prevot, A. S. H.,
830   Baltensperger, U., Poulain, L., Wiedensohler, A., Sciare, J., Gros, V., Borbon, A., Colomb, A.,
831   Michoud, V., Doussin, J.-F., Denier van der Gon, H. A. C., Haeffelin, M., Dupont, J.-C., Siour, G.,
832   Petetin, H., Bessagnet, B., Pandis, S. N., Hodzic, A., Sanchez, O., Honoré, C., and Perrussel, O.:
833   Formation of organic aerosol in the Paris region during the MEGAPOLI summer campaign:
834   evaluation of the volatility-basis-set approach within the CHIMERE model, Atmos. Chem. Phys.,
835   13, 5767-5790, https://doi.org/10.5194/acp-13-5767-2013, 2013.

836   Zhao, M., Wang, S., Tan, J., Hua, Y., Wu, D., and Hao, J.: Variation of urban atmospheric
837   ammonia pollution and its relation with PM2.5 chemical property in winter of Beijing, China,
838   Aerosol Air Qual. Res., 16, 1378–1389, https://doi.org/10.4209/aaqr.2015.12.0699, 2016.

Atmospheric
Chemistry
and Physics
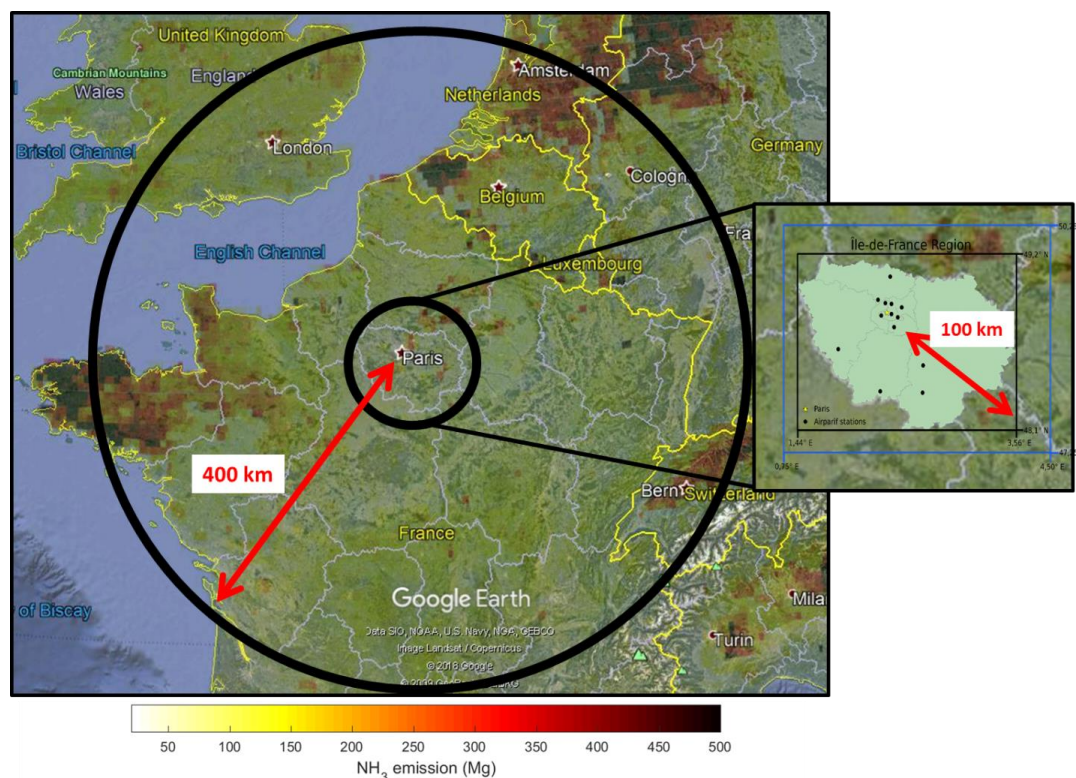Discussions

Open Access

839   Zhu, L., Henze, D. K., Cady-Pereira, K. E., Shephard, M. W., Luo, M., Pinder, R. W., Bash, J. O., and

840   Jeong, G.: Constraining U.S. ammonia emissions using TES remote sensing observations and the

841   GEOS-Chem adjoint model, J. Geophys. Res.-Atmos., 118, 3355–3368, doi:10.1002/jgrd.50166,

842   2013.

FIGURES

843

844

845 Figure 1: Region of analysis: 400 km radius-circle around the Paris megacity and 100 km around
846 Paris. The latter is representative of the Ile-de-France (IdF) region where the Airparif PM
847 observational network is located. Black points are the locations of the Airparif stations
848 measuring hourly $PM_{2.5}$ concentration at the surface. The black (blue) box delimitates the IdF
849 region in which the IASI NH_3 (ECMWF) data have been considered. The overlay represents NH_3
850 emissions (in Mg per year and per cell of 0.1°x0.1°) derived from the EMEP inventory for 2015.

851
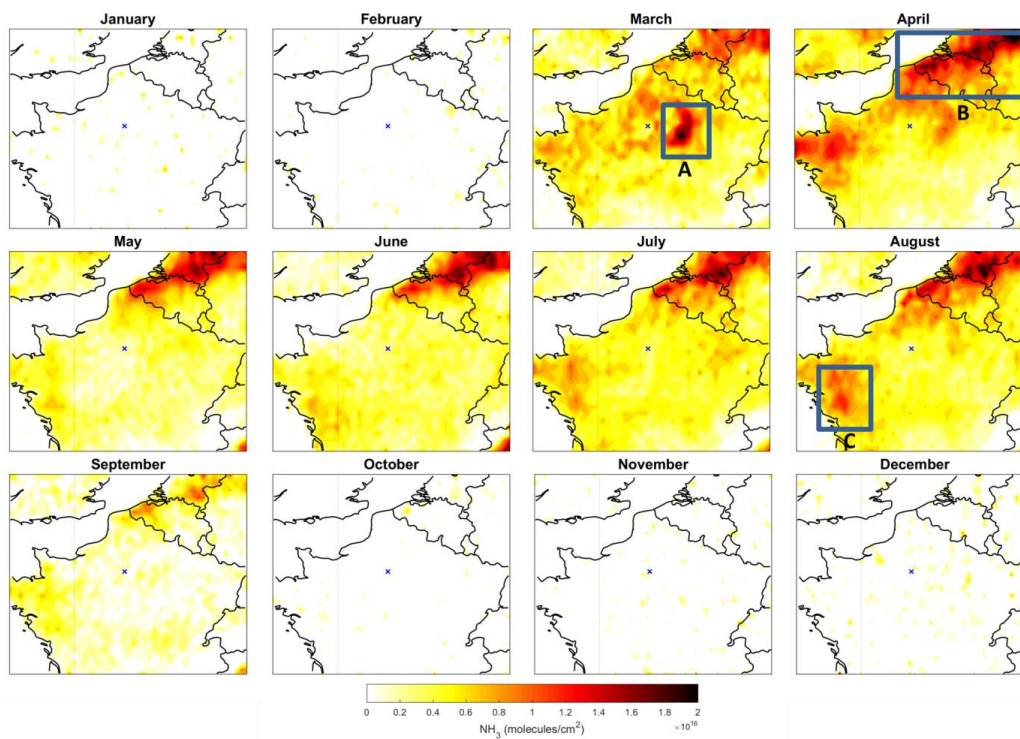
Figure 2: Monthly means of NH$_3$ total columns (molecules/cm²) derived from 10 years (2008-2017) of IASI NH$_3$-retrieved columns. The blue cross indicates Paris location.

854

855
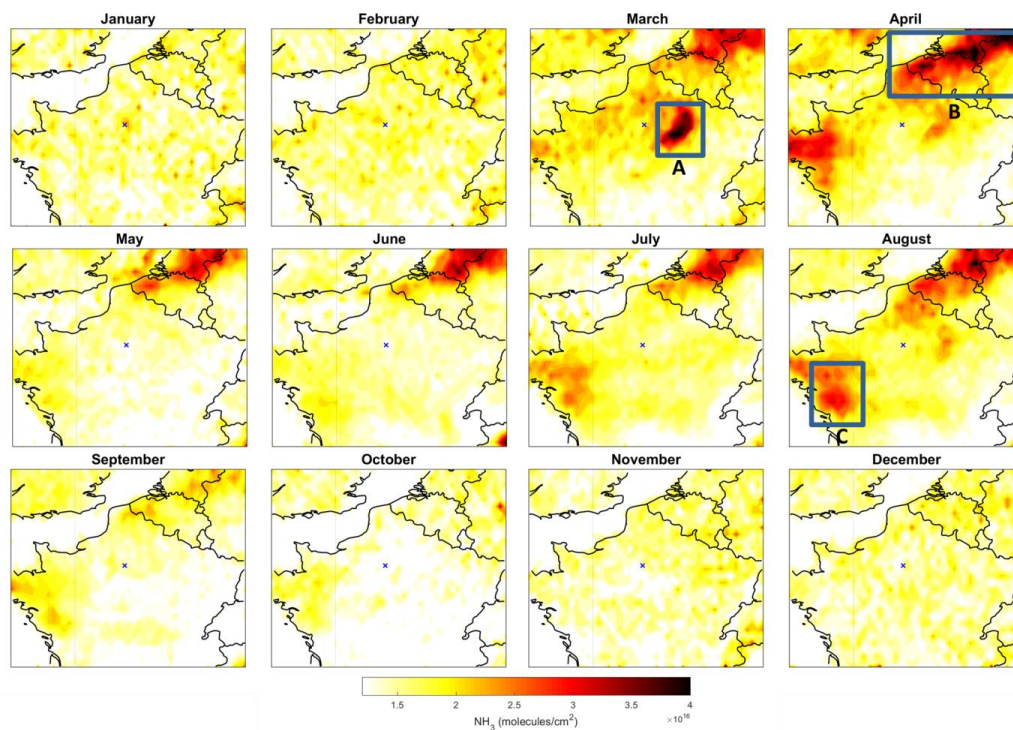
Figure 3: Monthly means of NH_3 total columns (molecules/cm²) derived from 5 years (2013-2017) of CrIS NH_3-retrieved columns. The blue cross indicates Paris location.
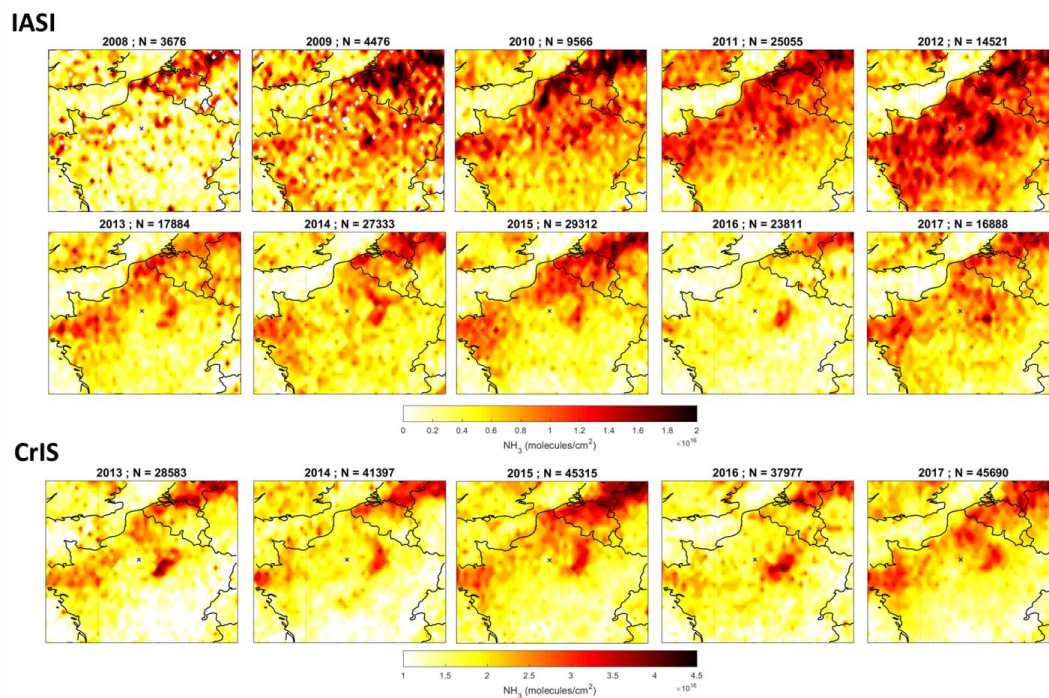
Figure 4: Maps of monthly mean NH_3 total columns (molecules/cm²) in March-April period derived from IASI from 2008 to 2017 and CrIS from 2013 to 2017.

861
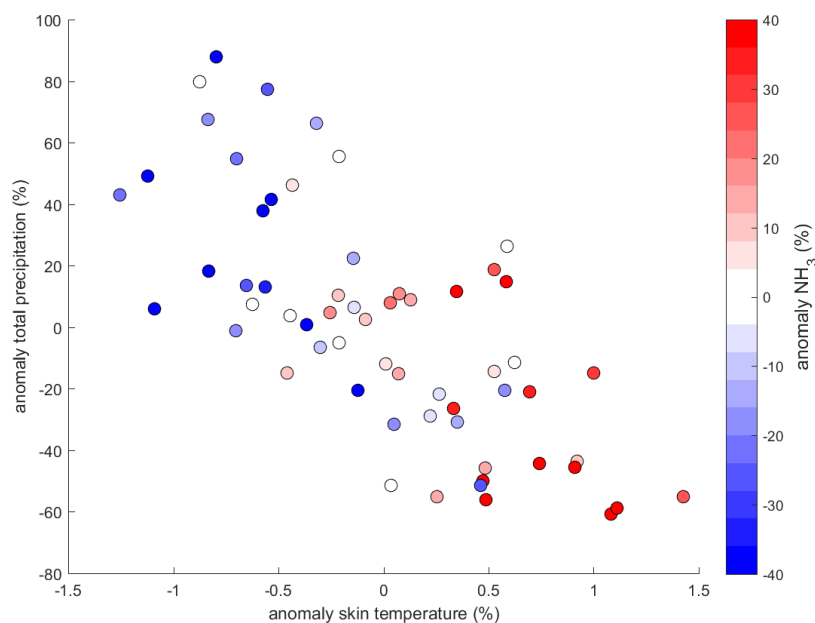
Figure 5: Scatter plot of monthly mean anomaly (relative to the 10-years – 2008 to 2017 -
monthly average) of total precipitation versus skin temperature derived from ECMWF from
March to August in the domain, and color coded by the NH₃ total columns anomaly derived
from IASI.
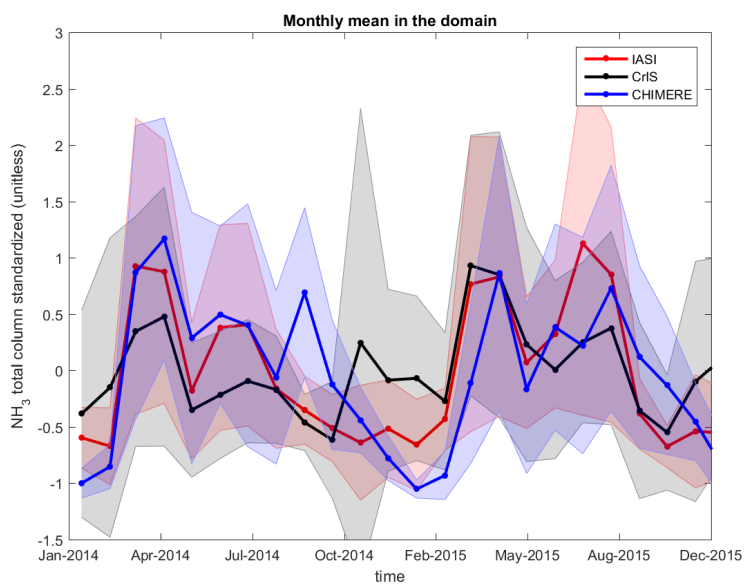
866

867 Figure 6: Standardized monthly mean concentrations derived from IASI (red), CrIS (black) and
868 CHIMERE (blue) for 2014 and 2015. Shaded areas correspond to the one-sigma standard
869 deviation around the means.

Atmospheric
Chemistry
and Physics
Discussions

Open Access

EGU

870
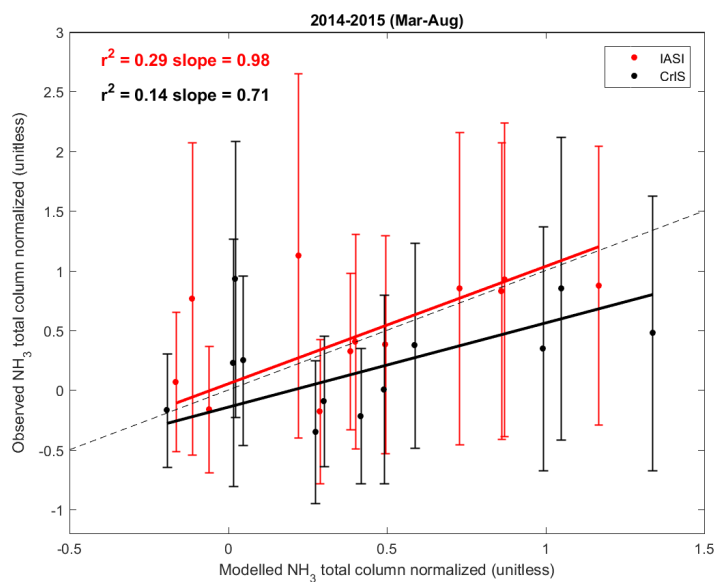
Figure 7: Correlation plots between monthly means NH$_3$ standardized concentrations derived from satellite observations (IASI in red and CrIS in black) and the CHIMERE outputs for the March to August months of 2014 and 2015. The 1:1 line is represented in the dashed line.

874
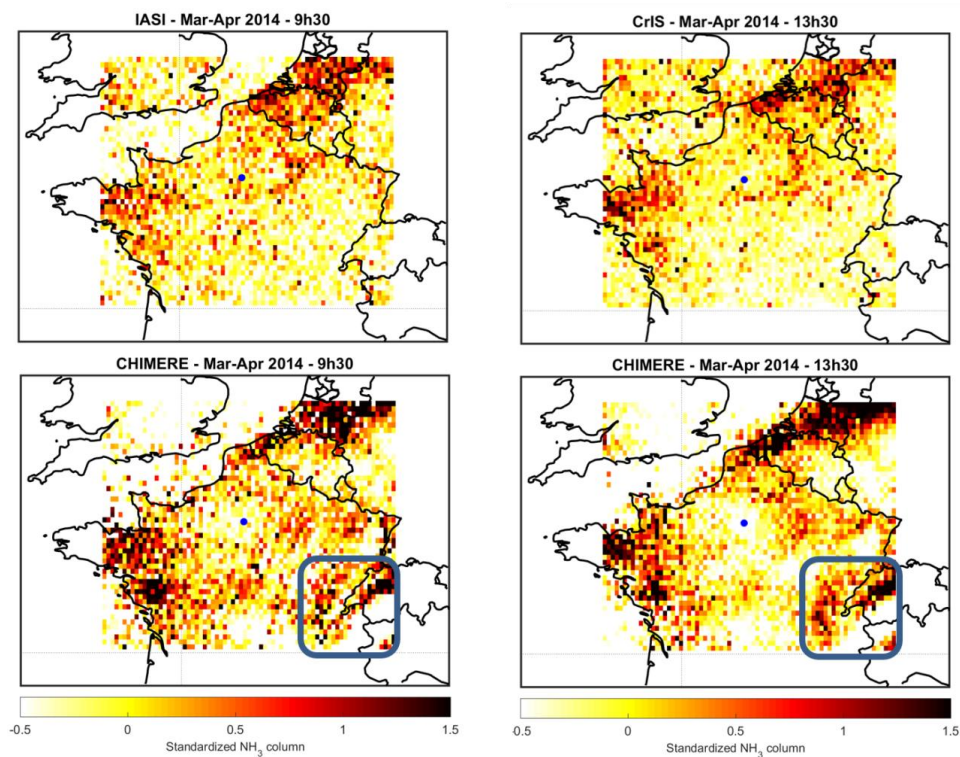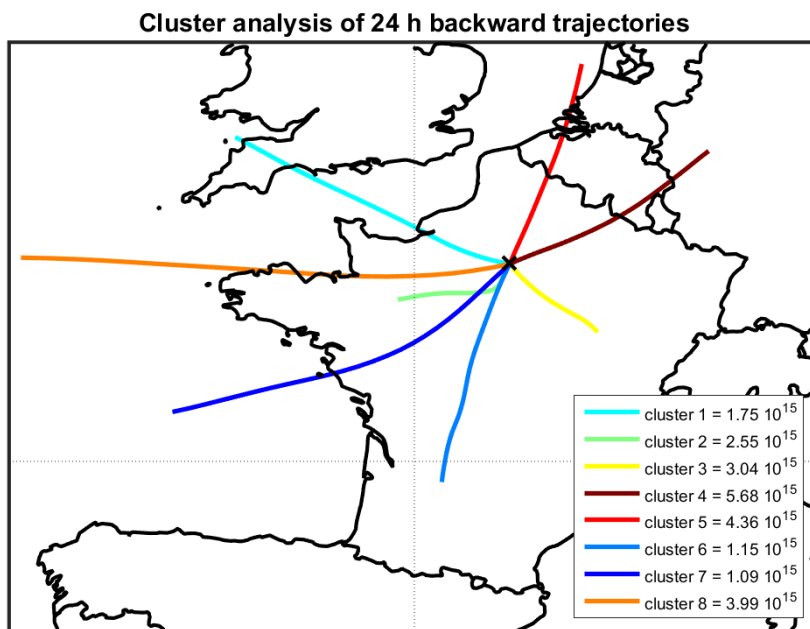
Figure 8: Standardized NH$_3$ column derived from the satellite instruments (IASI = top left panel, and CrIS = top right panel) and the corresponding NH$_3$ column derived from the CHIMERE model (coincident with IASI – bottom left panel, and coincident with CrIS – bottom left panel) for March-April 2014. Blue dots indicate Paris location.
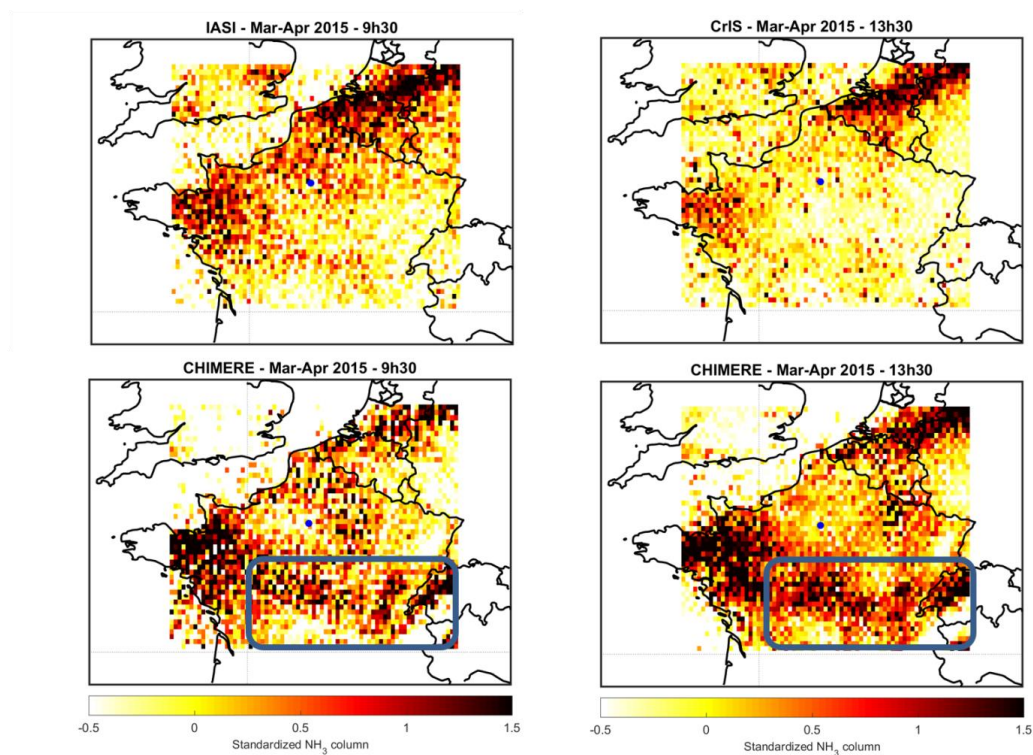
880   Figure 9: Same than Figure 7 but for March-April 2015.

Atmospheric
Chemistry
and Physics
Discussions

**Cluster analysis of 24 h backward trajectories**

881

882 Figure 10: Cluster analysis of 24-h backward trajectories arriving in spring in Paris (from
883 February 15th to May 15th for the 2013-2016 period) using HYSPLIT-4 model obtained from the
884 NOAA Air Resources Laboratory. Mean trajectories of the 8 clusters are shown in different
885 colors, associated with the NH_3 concentrations measured by IASI in the IdF region (in
886 molecules/cm^{-2}).

Atmospheric
Chemistry
and Physics
Discussions
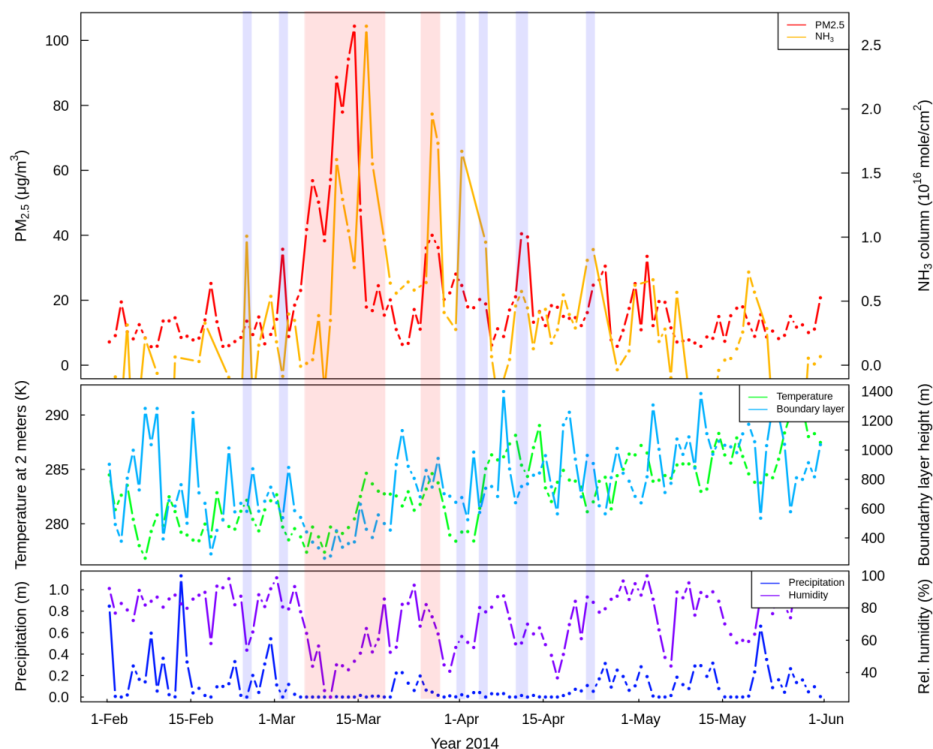
887
888 Figure 11: Average concentrations of NH$_3$ total columns derived from IASI (in molecules/cm²;
889 orange, upper panel) and PM$_{2.5}$ derived from the Airparif network selected within 2 hours from
890 the IASI overpass (in µg/m³; red, upper panel) for 2014 as example. Periods of simultaneous
891 (independent) enhancements of NH$_3$ and PM concentrations are represented with red (blue)
892 areas, i.e. case A (case B). Temperature at 2 meters (in Kelvin; green, middle panel), boundary
893 layer height (in meter; blue, middle panel), precipitation (in meter; dark blue, lower panel), and
894 relative humidity (in percent; purple, lower panel) derived from the ECMWF ERA-interim.
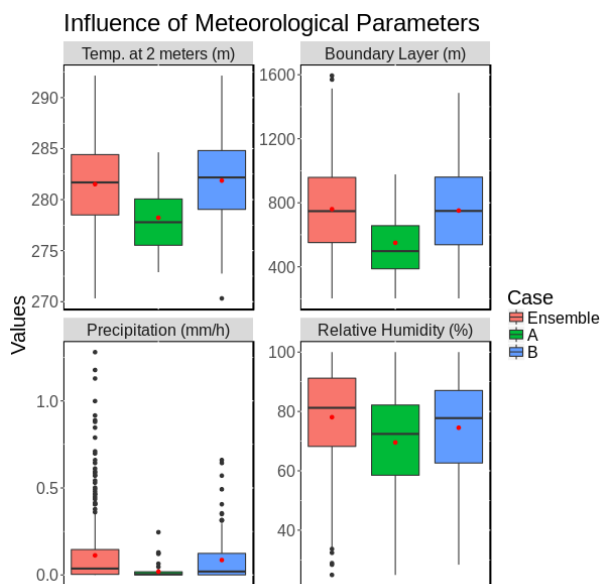
Figure 12: Statistical distributions of meteorological parameters corresponding to case A, case B, and all observations derived from 2013 to 2016. The medians and the quartiles are presented by center lines and borders of the boxes, respectively. The mean values are indicated by red points, and the extreme values (i.e. those beyond Q1 - 1.5 IQR and Q3 + 1.5 IQR) by black points.

900 **TABLE**

	Satellite	Overpass time (LT)	Time coverage	Nadir spatial resolution (km)	Spectral range (cm^{-1})	Spectral resolution (cm^{-1})	Spectral Noise[*] (K) @270K @ 970 cm^{-1}	References
IASI	Metop-A/B	9.30 (AM/PM)	2006-present	12	645–2760	0.5 (apodized)	~0.2	Clerbaux et al., 2009
CrIS	Suomi-NPP	1.30 (AM/PM)	2011-present	14	645–1095; 1210–1750; 2155–2550	0.625; (unapodized)	~0.05	Zavyalov et al., 2013

[*]Spectral noise comparison values in main ammonia spectral region (~970 cm^{-1}) obtained from Zavyalov et al., 2013.

901 Table 1: Instrumental specifications for the IASI and CrIS satellite instruments.